Author version: *Mar. Pet. Geol., vol.28; 2011; 1899-1914*

Fault system and thermal regime in the vicinity of site NGHP-01-10, Krishna-Godavari basin, Bay of Bengal

Dewangan, P.[*1], Sriram, G. [1], Ramprasad, T. [1], Ramana, M. V. [1] and Jaiswal, P. [2]

[1]National Institute of Oceanography, Goa, India

(Council of Scientific and Industrial Research)

[2]Oklahoma state university, Oklahoma, USA

[*]Corresponding author email: pdewangan@nio.org

Abstract

Drilling/coring activities onboard JOIDES Resolution for hydrate resource estimation have confirmed gas hydrate in the continental slope of Krishna Godavari basin, Bay of Bengal and the expedition recovered fracture filled gas hydrate at the site NGHP-01-10. In this paper we analyze high resolution multi-channel seismic (MCS), high resolution sparker (HRS), bathymetry, and sub-bottom profiler data in the vicinity of site NGHP-01-10 to understand the fault system and thermal regime. We interpreted the large scale fault system (> 5 km) predominantly oriented in NNW-SSE direction near NGHP-01-10 site, which plays an important role in gas hydrate formation and its distribution. The increase in interval velocity from the baseline velocity of 1600 m/s to 1750-1800 m/s within the gas hydrate stability zone (GHSZ) is considered as a proxy for the gas hydrate occurrence, whereas the drop in interval velocity to 1400 m/s suggest the presence of free gas below the GHSZ. The analysis of interval velocity suggests that the high concentration of gas hydrate occurs close to the large-scale fault system. We conclude that the gas hydrate concentration near site NGHP-01-10, and likely in the entire KG Basin, is controlled primarily by the faults and therefore has high spatial variability.

We also estimated the heat flow and geothermal gradient (GTG) in the vicinity of NGHP-01-10 site using depth and temperature of the seafloor and the BSR. We observed an abnormal GTG increase from 38^{o}C/km to 45^{o}C/km at the top of the mound, which remarkably agrees with the measured temperature gradient at the mound (NGHP-01-10) and away from the mound (NGHP-01-03). We analyze various geological scenarios such as topography, salinity, thermal non-equilibrium of BSR and fluid/gas advection along the fault system to explain the observed increase in GTG.. The geophysical data along with the coring results suggest that the fluid advection along the fault system is the primary mechanism that explains the increase in GTG. The approximate advective fluid flux estimated based on the thermal measurement is of the order of few tenths of mm/yr (0.37 – 0.6 mm/yr).

1. Introduction

Gas hydrate is an ice-like crystalline solid in which methane or other lighter hydrocarbon gases are trapped inside a cage of water molecules (Sloan, 1990). Gas hydrate is stable under high pressure-low temperature conditions and is formed when the methane gas dissolved in pore water exceeds its solubility limit. In marine sediment, gas hydrate occurs as vein filling, massive or nodular form or within the intergranular pore spaces (Helgerud et al., 1999). Under unstable conditions (high temperature-low pressure) gas hydrate dissociates and releases the trapped methane gas. This phase transition between the gas hydrate and free gas is known as the base of the gas hydrate stability zone (BGHSZ). The presence of gas hydrate within the sediments increases the velocity while free gas decreases the velocity thus creating a strong impedance contrast across the BHSZ. In seismics, the BHSZ is manifested as a seismic reflection commonly referred as the bottom simulating reflector (BSR; Hydnman and Spence, 1992; Singh et al., 1993; Helgerud et al., 1999). BSRs have been considered as one of the best proxy indicators for hydrate occurrence worldwide. Several gas hydrate related geophysical, geochemical and microbial proxies have been reported from the multidisciplinary investigations in the KG offshore (Ramana et al., 2006)

A collaboration program between Government of India and United States Geological Survey in 2006 for gas hydrate exploration led to multiple drilling/coring activities onboard R/V JOIDES Resolution around the continental margins of India. The expedition (NGHP-01), confirmed the presence of gas hydrate in Krishna-Godavari (KG) offshore basin (Collett et al., 2008). One of the sites, NGHP-01-10 shows ~128 m of elevated resistivity log response suggesting the presence of gas hydrates (Collett et al., 2008). The overall saturation of gas hydrate estimated based on the log and pressure core data is of the order of 25-30 % (Lee and Collett, 2009; Lee, 2009). Sediment core recovered from NGHP-01-10 site show fracture-filling gas hydrate. Furthermore, the X-ray images of pressure cores collected in the gas hydrate bearing sediment show that the hydrate is preferentially accumulated in the fractures (Collett et al., 2008). In a later experiment (May, 2007), the geological and geochemical analysis of a short sediment core (~30 m) acquired close to NGHP-01-10 site onboard Marion Dufresne show evidences of paleo-expulsion of methane rich fluids through the fault system and the presence of chemosynthetic clams like *Calyptogena spp*. (Mazumdar et al., 2009).

Hydrate accumulation can be structurally or stratigraphically driven (Milkov and Sassen, 2002). In structural accumulation gases are transported to the GHSZ through features such as faults and mud

volcanoes, e.g. northwestern Gulf of Mexico (Brooks et al., 1986; MacDonald et al., 1994; Milkov and Sassen, 2000, 2001; Sassen et al., 1999, 2001), Hydrate Ridge (Hovland et al., 1995; Suess et al., 1999, 2001; Trehu et al., 1999), and Haakon Mosby (Bogdanov et al., 1999; Ginsburg et al., 1999). In stratigraphic accumulation gases are transported along permeable horizons, e.g., Blake ridge (Xu and Ruppel, 1999; Dickens et al., 1997), Gulf of Mexico minibasins (Milkov and Sassen, 2001; Pflaum et al., 1986), Nankai trough (Matsumoto et al., 2001), and Mallik (Dallimore et al., 1999). A combination of both structural and stratigraphic transport and trapping mechanisms are also possible (Diaconescu and Knapp, 2000; Diaconescu et al., 2001). The understanding of structural and/or stratigraphic origin of hydrate formation is important to understand its genesis, accumulation, distribution of gas hydrate and also to estimate its economic potential. In the present study, we used the high resolution 2D multi-channel seismic data to study the subsurface structures close to the known gas hydrate site (NGHP-01-10). Other geophysical datasets used to interpret shallow subsurface structures include high resolution sparker, sub-bottom profiler and bathymetry.

In the continental margins the formation and distribution of gas hydrate appears to be closely related with the fluid/gas flow from deeper region into the base of the gas hydrate stability zone (BGHSZ) that can perturb the geo-thermal gradient (Ruppel and Kinoshita, 2000). In passive settings, anomalous flow occurs through permeable pathways in the zones with rapid sedimentation and compaction that prevents the fluids to be expelled during sedimentation (Judd and Hovland, 2007). In active margins the anomalous flow is mainly due to compression tectonics. Perturbations in BGHSZ have been linked to anomalous fluid flow in literature (Minshull and White, 1989; Davis et al., 1990; Zwart et al., 1996; Mann and Kukowski, 1999; Pecher et al., 2009). It is also a common practice to use BSR derived heat flow to understand the thermal profile along the continental margins (Davis et al., 1990; Fisher and Hounslow, 1990; Hyndman and Davis, 1992; Ashi and Taira, 1993; Townend, 1997; Ganguly et al., 2000; Kaul et al., 2000). In this study, we estimate the geothermal gradient (GTG) from the BSR depth to understand the thermal regime around NGHP-01-10 site. We have identified zones of abnormal GTG and made an attempt to understand the origin of these observed abnormal GTG through the integrated interpretation of different geophysical datasets.

2. Study Area

Krishna-Godavari (KG) basin is one of the petroliferous basins located in the middle of eastern continental margins of India (ECMI) extending from Vishakhapatnam in the north to Ongole in south

(Fig. 1). The ECMI evolved due to the separation of India from East Antarctica around 132 Ma, and subsequently resulted in the formation of three prominent basins namely Cauvery, KG, and Mahanadi (Powell et al., 1988; Scotese et al., 1988; Ramana et al., 1994). The KG basin is predominantly drained by rivers Krishna and Godavari that deposit the bulk of detrital sediment. The sediment thickness in the basin has found to exceed 8 km in some of the offshore depocenters (Prabhakar and Zutshi, 1993). The stratigraphy of the KG basin comprises Cretaceous to Recent sediments (Rao, 1993; Rao, 2001). The sedimentation rate varied throughout the geological time, but increased dramatically after the upliftment and erosion of Himalayas during the Neogene period (Subrahmanyam and Chand, 2006).

A characteristic feature of the KG basin is shale tectonism (Vijayalakshmi, 1988; Rao and Mani, 1993; Rao, 1993; Bastia, 2006; Gupta, 2006), a gravity-driven tectonic activity induced by movement of thick sediment mass over deeply buried mobile/overpressure shale strata (Damuth, 1994; Wu and Bally, 2000). The mobile/overpressured shale strata are known to exist in KG basin in Upper Cretaceous, Paleocene, Eocene and Miocene sequences (Rao and Mani, 1993). The Miocene and Pliocene growth faults have caused large anticlinal structures by triggering shale tectonics in the underlying shale sequences (Gupta, 2006; Ramana et al., 2009). The regional seismic lines in the KG basin (cf. Fig. 8 in Bastia, 2006) show significant deformation in the form of normal and thrust faults in deeper water (> 800 m water depth). In KG offshore basin, several bathymetric mounds are formed due to this deformation tectonics (Ramana et al., 2009; Dewangan et al., 2010). The analyses of bathymetry, high resolution sparker, sub-bottom profiler, and multi-channel seismic (MCS) data reveal that these bathymetric mounds are heavily faulted and provide conducive environment for the movement of fluid/gas. Bathymetric mounds resulting from toe-thrust faults/shale diapirism are potential zones for the gas hydrate accumulation and cold seeps (Dewangan et al., 2010). The present study area (Fig. 1) encompasses one such mound below which the gas hydrate presence is confirmed by drilling/coring operation.

3. Data and Methodology

About 100 line km of multichannel seismic reflection (MCS) data were processed and interpreted for BSRs in the vicinity of NGHP-01-10 (Fig. 1). The MCS data was acquired by the Oil and Natural Gas Commission Ltd. (ONGC) using 1000 cu. in. air gun fired at every 12.5 m and a 1.5 km long streamer (120 channels, 12.5 m group interval) were deployed to acquire the MCS data. The

shortest source-receiver distance was 75 m, and the recording length kept at 4 s. The data was recorded with 1 ms sample interval, with a high cut anti-alias filters set at 500 Hz.

The primary aim of MCS data processing is to enhance the ratio of primary reflections to ambient noise, and to provide a structural image through migration of the data. MCS data processing has been carried out following the standard methods emphasizing on deconvolution to remove the source bubble effects and normal and dip move-out velocity analyses. Other modules include trace editing, filtering, stacking, and post-stack time migration sequentially. Typically in marine datasets, multiples are a serious concern. However, in the present study, the seafloor multiple zone (> 2.67 s) occurs after our zone of interest due to the deeper depth of the seafloor (~1000 m). Twelve seismic profiles, each ~8 km in length, were processes independently. The time sections were converted to depth sections using stacking velocities. The seafloor and BSRs were picked on both time and depth sections after analyzing inline and crossline misties. Besides, 2-D nature of seismic processing, misties could occur due to anisotropy that is currently not accounted for. Misties are minimized by stretching the crossline profiles to match the inline profiles. The picked horizons were interpolated into three-dimensional surfaces.

Multibeam data acquired onboard Sagar Kanya (SK-176; 2002) was used to extract information on seabottom topography. Surface expression of faults and folds can be seen from the bathymetric mosaic. The public domain software for Multibeam System 4.6.10 (Caress and Chayes, 1996) has been used to process and grid the swath bathymetry data. The GMT Software has been used to generate the color-coded contour maps on IBM P275 workstation with AIX 5.3 operating system.

The sub-bottom profiler (SBP) data was acquired onboard Marion Dufresne (MD161; 2007) using Seafalcon 11 echosounder. One of the main features of this profiler is the use of a large dedicated transmission array, large bandwidth signal and long size multibeam reception array to create a high acoustic level signal and a very narrow beam-width. SBP data were processed using seismic processing software “ProMAX” to generate enhanced seismic images, which aided in inferring the shallow subsurface structure and faults.

High Resolution Sparker (HRS) data was acquired onboard Sagar Nidhi (SN21; 2009) using a 10KJ Geo-Resources Sparker system to understand shallow structures associated with the gas hydrate bearing sedimentary strata in KG Basin. The HRS data provided a maximum penetration of 400 m below the seabed. Frequency bandwidth of the dataset is between 150 and 1000 Hz with a dominant frequency of ~800 Hz for shallow reflectors (vertical resolution of ~46 cm), ~400 Hz for intermediate

reflectors (vertical resolution of ~92 cm) and ~250 Hz for deeper reflectors (vertical resolution of ~1.48 m). HRS data is processed using Promax software following the standard routines emphasizing on deconvolution, trace editing, filtering, and AGC.

Geothermal gradient was computed from the depths and temperatures of the seafloor and BSR. The seafloor temperature was obtained by using the available Conductivity-Temperature-Depth (CTD) profiles in the study area. It was established that the dominant gas in the gas hydrate of KG basin is the methane of biogenic origin (Collett et al., 2008). The phase curve of methane hydrate and sea water was obtained from the empirical formula of Miles et al (1995). The temperature at the BSR depth was obtained by considering the phase curve and the seafloor temperature assuming that the BSR depth corresponds to the base of the methane hydrate stability zone (MHSZ). The geothermal gradient (GTG) was calculated from the above parameters using the equation:

$$GTG = \frac{(T_{bsr} - T_{sf})}{(Z_{bsr} - Z_{sf})}, \qquad \text{(eq. 1)}$$

where Z and T represent the depth and temperature respectively and the subscript *bsr* and *sf* corresponds to the BSR and seafloor respectively. The heat flow 'q' was calculated by multiplying GTG with the average thermal conductivity (0.82 W/mK) of the sediment as,

$$q = k_{avg} \times GTG \qquad \text{(eq. 2)}$$

where K_{avg} and GTG represent the average thermal conductivity and geothermal gradient. The thermal conductivity of the sediment cores was measured during the drilling (Collett et al., 2008).

4. Interpretation

The shaded relief map of multibeam swath bathymetry along with the seismic lines is shown in Fig. 1b. Altogether twelve seismic lines were interpreted in the present study. All NNW-SSE lines are referred as inline, while the ENE-WSW lines as crossline. Interpretation of two mutually perpendicular seismic sections (migrated) that cross the NGHP-01-10 site are shown in Figs. 2 and 3. Main horizons and several faults are interpreted on all the lines for stratigraphic correlation across the faults. All horizons show distinct throws across the faults (Figs. 2 and 3); however, they appear to be heavily disturbed between the CDPs 750 to 950 in the inline profile. The orange horizon in particular has been used as a marker horizon. The acoustic basement (bottom most reflector) is associated with high amplitude and reverse polarity, representing the horizon with free gas. One of the interesting features in the seismic

profile is the presence of prominent positive topography feature corresponding to a mound, which occurs between CDPs 450 and 700, and bounded by the faults F_1 and F_3. The mound is identified in all seismic profiles and seen extending in a NNW-SSE direction over a length of >5 km. A series of normal faults (F_2-F_5) have been identified in the inline profile (Fig. 2c). The apparent dip of these faults is ~ 33^o, and all these faults orient in a SSE direction. However the fault F_1 dips ~ 47^o, and orient in the NNW direction with a throw of ~30 m. On the other hand, the faults F_2-F_5 are not characterized by appreciable throws. The migrated and un-interpreted crossline seismic section and the corresponding interpretations are shown in Fig. 3. The same horizons are mapped in this seismic section along with the major fault system (F_1-F_5). The apparent dip of the faults F_2-F_5 is ~ 64^o and orient towards ENE direction however faults F_1 dips ~ 60^o, and orient in the WSW direction. The mound bounded by the faults F_1 and F_3 is observed between CDPs 750 and 820. A subsurface pierced structure of approximately 60 m width at around 1.7 s is observed between CDPs 250 and 350. The horizons appear to be disturbed between CDPs 550 and 900, and difficult to trace. In such a scenario, the mistie between the inline and crossline components is used as a guiding factor to pick the horizons.

4.1 Fault pattern and related structures

The fault bounded positive topography feature interpreted from the seismic images has been designated as a mound, and this feature extends over ~5 km in a NNW-SSE direction (Fig. 1b). The mound has a relief of ~30 m from the surrounding seafloor, i.e., it rises to < 1020 m water depth from the surrounding 1050 m depth contour The width of the mound increases towards SSE direction and attains a maximum width of 500 m. The seafloor is picked from all the seismic lines and a 3D map is generated using the standard triangulation method (Fig. 4a). The major faults F_1-F_5 shown in Figs. 2c and 3c are picked from seismic lines and the trace of the fault system is plotted on the 3D seafloor map. The imprint of the fault system (though the faults (F_1-F_5) are sub-parallel) is distinctly visible on the mosaic, and the fault system exhibits a dominant NNW-SSE alignment. The orange horizon which has a distinct wavelet is picked on different seismic profiles and a contour map is prepared (Fig. 4b). The trace of the fault system along with NGHP site locations are plotted for comparison. The imprints of major faults F_1 and F_3 are reflected on the contour map whereas the imprint of other faults is relatively subdued. Further, the sites NGHP-01-10/21/12/13 where the presence of gas hydrate confirmed by drilling (Collett et al., 2008) are also shown in Fig. 4a with reference to the interpreted fault system. The NGHP-01-10 site passes through the fault F_4 whereas the other sites (NGHP-01-12 and NGHP-01-13) are close to the fault F_5. Even though the wells are located close to each other they are passing through

different geological environment due to the heterogeneity created by the fault system. This emphasizes the significance of faults in controlling the gas hydrate formation and occurrence. The SBP images close to the observed topographic mound are shown in Fig. 5. The sections across the northern, central, and southern segments of the observed topographic mound are shown in figure 5. The structures and characteristics of reflection echoes in the SBP data depict two distinct reflection patterns: i) parallel continuous reflectors associated with the mound, and ii) acoustically transparent zone with semi-prolonged bottom echo and regular overlapping hyperbolae (Fig. 5a) corresponding to the mass transport deposits (Pratson and Laine, 1989). These sediment deposits are conformable to the seafloor and onlap onto the mounded finely layered sediment. The SBP records (Fig. 5a) also depict the surface expression of the major faults (F_1, F_3 and F_4). The faults have uplifted the seafloor by about ~30 m to form a distinct bathymetric mound on the seafloor. The NGHP-01-10 site is located close to the major fault F_4 (Fig. 5a). In the southern part, the faults (F_1 and F_3) have risen the sediment block by 20-30 m; debris is observed on either side of the fault. No internal layering is observed within the raised horst structure. The width of the fault system is seen to be increasing from north to south (Fig. 5).

4.2 Gas hydrate accumulation style

A seismic event can be recognized as BSR if it: a) mimics the seafloor, b) exhibits reverse polarity with respect to seafloor, and c) crosscuts the sediment strata. Based on this criteria, we identified BSR (Figs. 2 and 3) between CDPs 250 and 900 (inline) and between CDPs 400 and 950 (crossline). The well at NGHP-01-10 site that recovered massive hydrate passes through fault F_4 (Fig. 3) on the processed seismic section. The stacking velocity is obtained from the conventional semblance analysis of multi-channel seismic data. The stacking velocity is assumed to be the RMS velocity and it is converted to interval velocity using Dix equation (Figs. 2d and 3d). The average background velocity is inferred as 1600 m/s within the gas hydrate stability zone based on the baseline velocity calculated from the simplified three-phase Biot equation in the NGHP-01-10 site (Lee, 2009). A drop in interval velocity to ~1400 m/s from this background velocity is observed below the BSR suggesting the presence of free gas below the BSR. Several high interval velocity patches (1750-1800 m/s) is observed above the BSR. These high velocity zones are due to the presence of gas hydrate. This increase in interval velocity is not uniform but occurs in patches showing large vertical and lateral variations in velocity. A pierced structure (Fig. 3c) is recognized in the interval velocity profile by the increase in velocity above this feature. The BSR amplitudes are normalized with respect that of seafloor and the result is shown in Figs.

2b and 3b. It is interesting to note that the amplitude of the BSRs increases from 20 % to about 60 % of the seafloor amplitude close to the fault system.

The HRS data with dominant frequencies of 150-1000 Hz close to the inline and crossline seismic profiles are illustrated in Fig. 6. The interpreted faults form the MCS lines are superimposed on the HRS sections. Almost all the inferred faults on the MCS sections are traceable on the HRS sections. The BSRs seen on the MCS data could not be traced on the HRS sections, and this may be due to the diminished amplitudes of BSR beyond the detectable limits. However, along few HRS sections we identified a faint reflector which corresponds to BSR time. Seismic blanking which is defined as the reduction of acoustic impedance between layers owing to the presence of gas hydrate in marine sediment (Lee and Dillon, 2001) is commonly observed in HRS data in the study area (between CDPs 650 and 950; 600 and 720 in Fig. 6). This blanking zone coincides with the region of fault system (F_3-F_5).

5. Geothermal Gradient

A proportional decrease in the seafloor temperature from 6.6 to 5.8 ^{o}C is observed with the increase of seafloor depth from 1000-1200 m in the study area. The seafloor temperature is derived from the CTD profiles (Fig. 7). In the present study, the depth to the BGHSZ in general corresponds to the depth of occurrence of BSR. We also assume the pressure at the BSR depth to be more or less equivalent to the hydrostatic pressure. The temperature at the BSR depth was estimated with the help of the phase curve of methane and standard seawater with 35 ppm salinity (Miles et al., 1995). Finally the GTG and the heat flow were computed using equations (1) and (2) respectively.

The GTG was computed for individual seismic profiles (Fig. 2b and 3b). Along inline seismic profile (Fig. 2b), we observe an increase in GTG from 40 ^{o}C/km to about 45 ^{o}C/km between CDPs 700 and 1000. The observed GTG is higher close to the fault system F_3-F_5 (Fig. 2c), and likewise, along crossline seismic profile (Fig. 3b), the GTG is increasing from 38 ^{o}C/km to 45 ^{o}C/km between CDPs 650 and 850 close to the fault system. In a similar fashion, the GTG is calculated in all twelve processed seismic lines (Fig. 8). The GTG seen increasing from ~38 ^{o}C/km to ~45 ^{o}C/km towards the top of the mound. The GTG distribution is asymmetric with respect to the seafloor topography (Fig. 8a). However, over the gas bearing horizon and the fault system the GTG distribution appears to be symmetric (Fig. 8b). From this sort of symmetry, it is obvious that the migration of fluid/gas through the fault system controls the distribution/accumulation of gas in the sediments. The maximum GTG anomaly is observed

at the top of gas bearing horizon and not at the top of seafloor mound. Therefore, the seafloor mound is formed due to the upliftment of seabed due to pushing of enormous gas through the fault system.

The mean thermal conductivity of the shallow sediment (< 200 m) at site NGHP-01-10 is about 0.82 W/mK (Collett et al., 2008). The variation of the measured thermal conductivity in the shallow sediment is small (standard deviation of 0.04) and the presence of hydrate show least influence on the bulk thermal conductivity (Grevemeyer and Villinger, 2001). We therefore ignored the minor variations in thermal conductivity and estimated the heat flow (by taking the product of mean thermal conductivity and the BSR-derived GTG). The heat flow in this region showed an increase from 31.16 W/m^2 to about 36.9 W/m^2 towards the center of the mound.

6. Discussion

6.1 Gas hydrate formation mechanism

In KG offshore basin, the methane hydrate mainly occurs either in a massive form or as fracture filling material in clay dominated sediment (Collett et al., 2008). The direct evidence of the fracture-filling gas hydrate is obvious from the X-ray images of the pressure cores. The analysis of LWD images, resistivity and velocity logs of NGHP-01-10 site suggests the presence of gas hydrate filled high angle faults (Collett et al., 2008; Lee and Collett, 2009). In a nearby site (NGHP-01-5), Cook and Goldberg (2008) have also shown that the gas hydrate occurs in high angle fractures. The presence of fractures increases the secondary porosity and permeability of the sediment and result in focused fluid flow which increases the likelihood of gas hydrate formation (Ruppel and Kinoshita, 2000). Large scale fractures/faults can be formed in the hydrate stability zone due to excess gas pressure at the BGHSZ or due to tectonic activities (Milkov and Sassen, 2000). At the same time, small planar fractures can be formed in the overburden due to the conversion of gas into gas hydrate (Cook and Goldberg, 2008). The fractures formed due to tectonic activity are regional and therefore, the gas hydrates are likely to be accumulated in large areas. If suitable environmental condition exists for such gas hydrate deposits, its economic potential will be high. On the other hand, if the fractures are created due to the formation of gas hydrates, its accumulation will be localized. Hence the exploitation of gas hydrate under such varied environment is a big challenge. Therefore, it is important to know the mechanism of fracture formation and gas hydrate accumulation. Near site NGHP-01-10, we have identified major fault systems (F_1-F_5) extending from more than 200 m deep from the surface (Figs. 2 and 3). Though the faults appear to

extend deeper, due to limited penetration obtained on MCS data we could image the faults only in the shallow overburden (< 200 m).

The contour map of the different horizons suggests that the faults are sub-parallel to each other and extend laterally to more than 5 km in the study area. The faults F_1 and F_3 have uplifted the sediment block by more than 30 m to create a prominent bathymetric mound. The lateral and vertical extent as well as the throw of the fault suggests that the fault system of this magnitude is primarily controlled by neo-tectonic activities. Similar fault systems have also been interpreted from the attribute analysis of 3D seismic data in KG offshore basin (Riedel et al., 2010). Therefore, we propose that the gas hydrate system in KG offshore basin is structurally controlled due to deformation tectonic activity.

6.2 Seismic characterization of gas hydrate bearing sediment

The occurrence of gas hydrate is inferred from the presence of BSRs, which are identified on the seismic profiles. The BSR appears to be continuous throughout the mound. At the same time the BSR shows varying amplitude, and is more prominent close to the interpreted fault system. The velocity obtained from conventional semblance analysis (Figs. 2d and 3d) show a drop in interval velocity below the BSRs suggesting the presence of free gas below the GHSZ. The free gas below the hydrate stability zone extends continuously below the mound and not confined to the faulted zones.

The presence of methane hydrate increases the velocity of the marine sediment (Helgerud et al., 1999; Singh et al., 1993). We observed, several patches of locally increased interval velocity (1750-1800 m/s) which are higher than the predicted baseline velocity (1600 m/s; Lee, 2009) in the study area suggesting the presence of hydrate in the stability zone. It is also interesting to note that high velocity patches occur in the vicinity of the interpreted fault system suggesting that the gas hydrate are preferentially distributed close to these fault system. The presence of gas hydrate is confirmed by drilling through fault F_4 (NGHP-01-10 site) where fracture-filling gas hydrate has been recovered. The other NGHP sites 12 and 13 located close to the fault F_5 show high-to-moderate gas hydrate saturation. However, NGHP site 21 located in between F_4 and F_5 show comparatively low gas hydrate saturation (Collett et al., 2008). The BSR amplitudes (Figs. 2b and 3b) depend upon the impedance contrast between the hydrate and free gas bearing sediment and are enhanced close to the major faults suggesting that the dominant presence of hydrate/gas in the vicinity of the faults.

Combining the drilling/coring results with seismic interpretation and velocity model, we propose that the likelihood of gas hydrate formation increases if the location is close to major faults. However,

there are other factors which may control the distribution of hydrate. For example, the pierced structure interpreted as mud diapir increases the velocity indicating locally dispersed gas hydrate deposit. There are some high velocity patches that cannot be correlated with any observed geological structure. More seismic lines along with accurate velocity models are required for complete understanding of all geological factors. The analysis of BSRs and perturbation of interval velocity suggest that BSRs are formed due to the presence of free gas below the BHSZ and is observed throughout the diapiric mound; however, gas hydrate is mainly confined to the fault controlled geological set up in the KG offshore basin.

6.3 Variations in BSR-derived geothermal gradient

Indirect estimation of geothermal gradient (GTG) and heat flow from the depth of the gas hydrate stability zone have been used to understand the thermal regime of the continental margins (Hyndman and Davis, 1992; Grevemeyer and Villinger, 2001). The heat flow (q) primarily depends on the age of the crust (Stein and Stein, 1994) and can be calculated as,

$$q = 48 + 96 * e^{-0.0278*t} \qquad \text{(eq. 3)}$$

Where t represents the age of the crust in million years before present and the equation is valid for t > 55 ma. The study area is located close to M11 magnetic anomaly zone (Ramana et al., 1994); hence we can assume the age of the crust to be ~ 130 Ma. Substituting the value for age of the crust in equation (3), we obtain the background heat flow to be about 50 m W/m^2. The heat flow shows significant dependence on the nature of sediments, the sedimentation rate and age of the sediment (Hutchison, 1985). Assuming clay-dominated sediment (Collett et al., 2008) and a sedimentation rate of ~ 20-30 m/Ma, the correction factor will be of the order of 35-40 %. After accounting the correction due to sediment, we estimate the background heat flow to be in the range of 30 -32.5 m W/m^2. The background GTG estimated from heat flow assuming mean thermal conductivity of 0.82 W/mK will be about 36-40 ^{o}C/km.

In the study area, we observed a similar background GTG of about 38-40 ^{o}C/km which increases by a factor of 15-20 % to about 45 ^{o}C/km towards the top of the mound close to the fault system. The insitu temperature was measured at selected depth using Davis-Villinger temperature probe onboard JOIDES Resolution and GTG was estimated from regression analysis (Collett et al., 2008) on the top of the mound (Fig. 1b; NGHP-01-10) and away from the mound (Fig. 1b; NGHP-01-03). The estimated GTG remarkably agrees with this BSR-derived GTG. For example, the depth of BSR at site NGHP-01-

10 obtained from the seismic section is about 157 mbsf which is close to that recorded from the logging data. The seafloor temperature at site NGHP-01-10 is about 6.46 ^{o}C from the available CTD profiles. The temperature at the depth of the BSR is about 13.38 ^{o}C from the methane + seawater phase curve. Thus, the geothermal gradient at site NGHP-01-10 calculated from equation (1) is 44.1 ^{o}C/km. The downhole temperature (Collett et al., 2008) measured at this site implies a geothermal gradient of 45 ± 3 ^{o}C/km and a seafloor temperature of 6.5 ± 0.3 ^{o}C which are close to the estimated values. The estimated GTG from downhole temperature measurements at NGHP-01-03 site, which is located 8 km away from the NGHP-01-10 site (Fig. 1b), is 39 ± 2^{o}C/km representing the background GTG.

BSR-derived GTG may differ from the actual GTG due to uncertainty in calculation of phase curves if the gas composition of the hydrate is not known, uncertainty in calculating the bottom water temperature, inaccuracy in estimating the depth of the reflectors due to unavailability of velocity structure or errors in velocity model, and error in BSR depth estimation due to seismic anisotropy. Moreover, such discrepancies may also occur if the BSR depth does not correspond to the BGHSZ due to capillary forces arising in fine grained sediment (Ruppel, 1997; Hovland et al., 1997). Additional errors in heat flow estimate may come from the uncertainties in estimating thermal conductivity and the effect of gas hydrate on thermal conductivity (Grevemeyer and Villinger, 2001). In the following sections, we try to evaluate the error in BSR-derived GTG under the constraints of drilling/coring data.

6.3.1 Uncertainties in prediction of GHSZ

The gas obtained from the dissociation of pressure cores collected in KG offshore basin is predominantly methane of biogenic origin (Collett et al., 2008); hence the phase curve of methane + seawater is appropriate for predicting GHSZ. In general, the thickness of the GHSZ calculated from the temperature data acquired during the expedition and the phase curve of pure methane + seawater system agrees with the BSR depth recorded on the log data suggesting that the base of the GHSZ coincides with the depth of BSRs (Collett et al., 2008). Since the calculated GTG is close to the observed GTG we can assume that the gas hydrate is in thermal equilibrium and the base of the methane hydrate stability zone corresponds to BSR; therefore the effect of capillary forces is negligible.

6.3.2 Errors due to inaccurate velocity models

The presence of gas hydrate increases the seismic velocity (Singh et al., 1993). In building the velocity model, if the velocity of hydrate layers is underestimated then it will lead to underestimation of depth of BSR and hence overestimation of GTG. The velocity errors increase significantly if the offset-to-depth

ratio is less than unity. In the present study, the offset-to-depth ratio is close to 1.5 hence we can expect reasonable accuracy in estimating Normal Moveout (NMO) velocities. The following simulation was carried out to test whether the error in velocity can generate the observed anomaly in GTG. The CDP gather was corrected with the constant velocity (1510 km/s) required to produce desired GTG values. If the GTG is assumed to be known, we can calculate depth of the BSR and hence the interval velocity between the seafloor and BSR which can be used to estimate the NMO velocity at the BSR depth. The NMO corrected CDP gather at the top of the mound with the velocity (1510 m/s) required for anomalous GTG (45 ^{o}C/km) is shown in Fig. 9a. Similarly, NMO corrected CDP gather with the velocity (1540 m/s) required to produce background GTG (40 ^{o}C/km) is shown in Fig. 9b. The velocity required for GTG (45 ^{o}C/km) produces a flat CDP gather at the BSR depth suggesting that the velocity is correct while a significant moveout is observed for the velocity required for background GTG. Therefore, the velocity errors cannot account for the observed variation in GTG. Furthermore, good agreement between BSR depth obtained from seismic and logging indicate that the velocity model is accurate enough for time-to-depth conversion. If we assume an error of ± 5 % in the interval velocity of gas hydrate bearing sediment, it will lead to ± ~1% error in NMO velocity and depth of BSR and ± 5 % error in GTG.

6.3.3 Errors due to seismic anisotropy

The gas hydrate in KG offshore basin appears to be distributed preferentially within the fault/fractures network in clayey sediment. If the fractures have preferred orientation then the medium becomes anisotropic (Tsvankin, 1997). In fact, the analysis of resistivity and logging data indicate that the correct estimates of gas hydrate saturation cannot be obtained if anisotropy is ignored (Lee and Collett, 2009). Due to anisotropy, the NMO velocity will be different from the vertical velocity which will lead to error in BSR depth and in turn estimated GTG.

In the present study, we have ignored the effect of anisotropy in time-to-depth conversion because the anisotropic model parameters are not known. Hence, we try to assess the errors in time-to-depth conversion due to anisotropy. If we assume that the observed fault system can be represented by a single set of vertical fractures then the medium can be approximated as Horizontal Transversely Isotropic (HTI) medium. The normal moveout velocity (V_{nmo}) of horizontal reflectors for such medium depends on the vertical velocity (V_{P0}), azimuth of the seismic line with respect to the symmetry axis (β) and Thomsen's parameters $\delta^{(v)}$ (Tsvankin, 1997; Contreras et al., 1999; Bakulin et al., 2000) and can be expressed as,

$$V_{nmo}(\beta) = V_{P0}\sqrt{\frac{1 + 2\delta^{(v)}}{1 + 2\delta^{(v)}\sin^2(\beta)}} \qquad \text{(eq.4)}$$

Along the strike direction of the fractures ($\beta = 90$), the incident and reflected rays lie in the isotropy plane and NMO velocity is equal to the vertical velocity. Under such a scenario, error will be negligible in time-to-depth conversion due to anisotropy. Along the dip direction of the fractures or along the symmetry axis ($\beta = 0$), NMO velocity differs from vertical velocity and the error is governed by the anisotropic parameter $\delta^{(v)}$. The value of the parameter $\delta^{(v)}$ is generally negative for the fractured medium therefore the NMO velocity will always be less than the vertical velocity (Tsvankin, 1997). Lee (2009) showed that the anisotropy parameters ($\delta^{(v)}$) depends upon the gas hydrate saturation (fracture density) and is approximately equal to -0.07 at site NGHP-01-10 assuming hydrate volume is 15 percent of total sediment volume. Using the parameters for site NGHP-01-10, vertical velocity in the GHSZ will have an error of 7% and overall vertical velocity (sealevel to BSR) will be underestimated by 1%. The underestimation of vertical velocity will lead to underestimation of depth by 1% and therefore overestimate the geothermal gradient by 7%. The error in GTG estimates in any other direction will be in between zero and 7%. We expect minimum error in GTG due to anisotropy for the seismic lines that are oriented close to the strike direction of the interpreted fault system (inline seismic profiles). In general, we observed that BSRs do not match in depth for the inline and crossline seismic section because of the velocity errors or anisotropy. The depth of BSR was forced to match at the tie location by artificially stretching the velocities of the seismic lines oriented along the dip direction in order to minimize the error in GTG. Therefore, we can assume that the average error in GTG due to anisotropy is about 3-4 %. The observed variation in GTG in the study area is about 15-20 % which is beyond the error introduced due to anisotropy.

6.4 Origin of abnormal GTG anomaly in the vicinity of NGHP-01-10 site

The geothermal gradient estimated from the analysis of high resolution multi-channel seismic data suggests an abnormal increase in GTG by 15-20 % over the bathymetry mound in KG offshore basin where the presence of gas hydrate is confirmed by drilling/coring. The abnormal perturbation of GTG may result from the focusing/defocusing of heat flow due to seafloor topography, variation in salinity at the base of the hydrate stability zone which can change the methane + seawater phase curve, thermal non-equilibrium of BSR and fluid/gas advection along the fault system. In this section, we try to analyses each of these factors to understand the origin of abnormal GTG perturbation.

The heat flow from the earth interior is distorted from the seafloor topography due to focusing and defocusing effect. In a purely conductive model, the focusing of heat flow in the valley intensifies the flux while defocusing of heat flow in the topographic mound decreases the heat flux (Lachenbruch, 1968; Ganguly et al., 2000). In general, the regional heat flow map derived from the 2D seismic survey in KG offshore basin shows that the overall trend in BSR-derived heat flow across major topographic features corresponding to the expected trends from topographic modeling (Shankar and Riedel, 2010). In order to understand the topographic effect on GTG in the study area, we have utilized the analytical solution provided by Lachenbruch (1968). In this model, the irregular seafloor topographic surface is replaced by a series of plane reference surfaces. For a plane slope of height H and angle β (between 0 and $\pi/2$), the heat flow $q(x)$ at a distance x from brink of the slope is given by:

$$q(x) = G(1 + \Delta q(x))$$

$$= G\left(1 + \frac{1}{\pi}\tan\beta \ln\left[\frac{x}{x + H\cot\beta}\right]\right) \qquad \text{eq. (5)}$$

where G is the background geothermal gradient. For inline seismic line (Fig. 2a), the seafloor topography can be approximated by two horizontal planes and a dipping plane (Fig. 10a). Assuming a regional GTG of 40^{o}C/km, we calculated the perturbation in GTG due to topographic effect (Fig. 10b). We observe that the topographic effect can distort the GTG by ±2 ^{o}C/km. However, the topographic correction cannot explain the observed GTG variations as it shows decrease in GTG at ridges and increase in GTG at valley contrary to the observed trend.

Therefore, the observed GTG anomaly in the study area is not due to the topographic effect.

The estimated GTG depends on the temperature, pressure and phase curve of methane + seawater. The phase curve of methane + seawater is depended on the pore water salinity due to the inhibition effect of pore water salinity on the gas hydrate stability (Sloan, 1990). High pore water salinity shifts the gas hydrate stability to lower temperatures and may also play a significant role in BSR shallowing as observed in the Blake Ridge diapir (Taylor et al., 2000). The interstitial pore water chloride fluctuates between 398 to 634 mM (Collett et al., 2008). The elevated Cl^- values in the gas hydrate zone represent the minimum estimate of the *in situ* Cl^-concentration as the gas hydrate dissociation lead to decrease in Cl^- concentration. Therefore, the possibility of perturbation of phase

curve due to increase in salinity exists in KG offshore basin. KG basin represents a passive continental margin where salt does not exist in the stratigraphy (Rao, 1993) thus we can rule out the possibility of brine from the deeper horizons. In order to estimate the salinity effect on GTG, we estimated the GTG (Fig. 11) assuming constant BSR depth but with varied phase curve of methane + seawater for a range of salinity values (35 g/l to 55 g/l) using CSMHYD software (Sloan, 1990). In order to explain the anomalous GTG at the top of the mound, the required salinity is ~ 50 g/l (~859 mM Cl^- concentration). Let's assume that the salinity increases is due to the formation of gas hydrate (25-30 % saturation), the resultant salinity in the surrounding pore water will be around 46-50 g/l. In theory, the anomalous GTG can be explained due to the increase in salinity resulting from the formation of gas hydrate.

Another possibility which can explain the observed GTG anomaly is the thermal non-equilibrium of BSRs. In general, the GTG can be estimated from the depth of BSR by assuming the thermal equilibrium state of BSR with the surrounding formations. However, the regions of rapid deposition and frequent landslides may result in thermal non-equilibrium state of BSRs, and thereby the estimated GTG may be erroneous. In the study area, we observe rapid sediment deposition in the form of debris flow between CDPs 200 and 500 (Fig. 2a) which may lower the estimate of BSR-derived GTG if the BSR in this region is in non-equilibrium state. Another possible mechanism for the abnormal perturbation of GTG is the fluid flow along the fault system. The similarity of GTG anomaly with the subsurface gas horizon further suggests that the GTG anomaly may depend on subsurface fluid flow through the fault system. Several studies elsewhere have shown similar increase in geothermal gradient due to focused fluid flow (Minshull and White, 1989; Davis et al., 1990; Zwart et al., 1996; Mann and Kukowski, 1999; Pecher et al., 2009). Therefore, the most favorable mechanisms that can explain the observed GTG anomaly are i) the increase in salinity resulting from the hydrate formation, ii) thermal non-equilibrium of BSRs due to rapid deposition at the flanks of the mound, or iii) the fluid flow through the fault system. The estimated GTG from the *in situ* downhole temperature measurements (Collett et al., 2008) at the top of the mound (site NGHP-01-10) and away from the mound (site NGHP-01-03) suggests that GTG actually increases by ~ 18 % towards the top of the mound. The agreement between the BSR-derived GTG and the measured GTG suggests that the estimated GTG anomaly is actual and not a biased GTG that resulted from neglecting the effect of salinity variation or the thermal non-equilibrium of BSRs. Therefore, we propose that the most likely mechanism which can explain the observed GTG anomaly is the fluid flow along the fault system. The preferential distribution of gas hydrate in the fault system (interval velocity model, X-ray image of pressure core, and sediment recovered from NGHP-01-

10 site) further corroborates this proposed mechanism. The focused fluid flow may be attributed to deformation tectonics in KG offshore basin (Dewangan et al., 2010; Ramprasad et al., 2011). The fluid flow along the fault system can be confirmed by geochemical analysis of pore water. For example, the fluid flow can be estimated from the Cl^-, Br^-, I^- ions concentration measured from pore water (Davie and Buffet, 2003). Although the Cl^- measurement was carried out at site NGHP-01-10 but it is largely affected by the dissociation of gas hydrate and therefore cannot be used to estimate fluid flux. The effect of gas hydrate can be minimized by taking the ratio of Br^- to I^- (Egeberg and Dickens, 1999) but we are not aware of any I^- measurement at site NGHP-01-10. Hence, we are unable to use geochemical parameters to confirm the hypothesis of fluid flux through the faults. The other option to estimate fluid flux is through chlorine isotope (Hesse et al., 2006), Boron, strontium isotopes (Deyhle et al., 2003) and Iodine isotope (Lu et al., 2008) which have the potential to provide direct estimate of fluid flux.

6.5 Fluid flux along the fault system

In order to estimate a first-order approximation of fluid flow rates in KG offshore basin, we follow the methodology as described by Land and Paull (2001), Hornbach, et al (2005), Arriaga and Leap (2006) and Pecher, et al (2009), which utilizes the variations in GTG. The methodology is based on the 1-D analytical solution of the differential equation for simultaneous conductive and advective heat transport in a homogenous and isotropic medium (Bredehoeft and Papadopulos, 1965). The depth dependent temperature profile (Tz) may be estimated as a function of Darcy velocity (v_d) from the solution of 1-D analytical equation (Appendix A),

$$\frac{T(z) - T(0)}{T(L) - T(0)} = \frac{e^{\beta z / L} - 1}{e^{\beta} - 1}\,;\ \beta = \frac{C_f \rho_f v_d L}{K_b} \qquad \text{eq. (5)}$$

where C_f and Δ_f represents the specific heat capacity and density of the pore fluid respectively and K_b is the bulk thermal conductivity of the sediment. One of the assumptions of this methodology is that the fluid flow due to normal pressure gradient may migrate in a dispersed way at low rates and they may not transport any significant heat compared to conductive heat flow. However, advective heat flow may become significant if the fluid flow is focused. Thus the methodology can be used to infer the flux of focused fluid flow either in the permeable horizon or in the fault system. In KG offshore basin, the fluid flow along the fault system is the most likely mechanism for the advective heat flow. The solution requires known temperature at three depth levels seafloor, BSR and a deeper horizon. We assume that the fluids may be advecting from overpressured formation of Upper Cretaceous, Paleocene, Eocene and

Miocene sequences. Assuming a sedimentation rate of 250-300 m/Ma, the base of these sequences is estimated to be about 5200, 4700, 4000 and 3000 m, respectively (Rao and Mani, 1993). The temperature at these depths can be obtained from the background GTG of ~40 ^{o}C/km. The other parameters required for the solution are listed in Table 1 (after Xu and Ruppel, 1999; Pecher et al., 2009). A range of temperature profiles for different overpressured sequences and Darcy velocities are shown in Fig. 12. We estimated the fluid advection rates for Upper Cretaceous, Paleocene, Eocene, and Miocene sequences, which are: ~0.37, ~0.4, ~0.5 and ~0.6 mm/yr, respectively.

The mechanism for free gas and BSRs formation can be broadly classified into hydrate recycling and solubility-curvature mechanism based on the upward fluid flow rate and shifting of hydrate stability zone due to burial or tectonic upliftment (Haacke et al., 2007; Haacke et al., 2008). The fluid advection rate in KG offshore basin (0.37-0.6 mm/yr) suggests that hydrate recycling will be the dominant mechanism for the formation of free gas due to high fluid flux similar to North Cascadia (Hyndman et al., 2001), Nankai trough (Baba and Yamada, 2004), Costa Rica (Pecher et al., 1998), Chile (Grevemeyer et al., 2003) and Hinkurangi margin (Pecher et al., 2009). Most of known sites of high fluid flux belong to accretionary wedges in active convergent margins. In contrast, the KG offshore basin is a rifted passive continental margin where sediment deformation due to toe-thrust faults/shale diapirism may have provided conducive environment for focused fluid flow.

7. Conclusions

The pressure cores and the log data of NGHP site 10 in KG offshore basin indicate that the distribution of gas hydrate is controlled by the fault/fracture system. We have shown the existence of regional fault system through the analysis of MCS and high-resolution seismic, bathymetry, and sub-bottom profiler data. The origin of such fault system can be explained by neotectonic activities; we attribute the fault system in the study area to deformation tectonics due to toe-thrust faults/shale diapirism. The gas hydrate is preferentially distributed along the fault zones as indicated by the interval velocity model. However, the BSR in the study area is observed throughout the mound and is formed due to the presence of free gas below the GHSZ. The geothermal gradient and hence the heat flow increases by a factor of 15-20% at the center of the mound compared to that at flanks. The abnormal increase in GTG at the center of mound is beyond the error introduced due to velocity uncertainty or anisotropy. We evaluated varied scenarios such as topography, salinity, thermal non-equilibrium of BSR and focused fluid flow and suggest that the most likely cause of the increased GTG is due to the

migration of deeply-originated fluid through the fault system. We estimated the fluid flux in KG offshore basin to be of the order of 0.37-0.6 mm/yr.

Acknowledgements We thank Director, National Institute of Oceanography (NIO) for supporting this study. We also extend our sincere thanks to oil industry for providing valuable seismic data, and A. V. Sathe (ONGC) and M. V. Lall (DGH) for their suggestions. The anonymous reviewers are thanked for valuable comments and suggestions for improving the manuscript. This is NIO contribution no. xxx.

Appendix A – Estimation of fluid advection rate

We estimate the fluid advection rate based on the thermal measurement as described by Land and Paul (2001), Arriaga and Leap (2006), and Pecher, et al. (2009). The partial differential equation for simultaneous transfer of heat and water assuming 1-D heatflow and incompressible fluids in a homogenous, isotropic and completely saturated porous medium is given by Stallman (1963) as,

$$\rho_b C_b \frac{\partial T}{\partial t} = K_b \frac{\partial^2 T}{\partial z^2} - \rho_f C_f \upsilon_d \frac{\partial T}{\partial z}$$

Where

ρ: density
C: specific heat capacity
T: temperature
t : time
K: thermal conductivity
Z: depth
v_d: Darcy (or filtration) velocity
indices –*f:* fluid, *b:* bulk sediment

For steady-state conditions, the time derivative goes to zero and the equation is simplified as,

$$K_b \frac{\partial^2 T}{\partial z^2} = \rho_f C_f \upsilon_d \frac{\partial T}{\partial z}.$$

The analytical solution to above equation was proposed by Brefehoeft and Papadopulos (1965) as,

$$\frac{T(z) - T(0)}{T(L) - T(0)} = \frac{e^{\beta z / L} - 1}{e^{\beta} - 1}, \qquad \beta = \frac{C_f \rho_f \upsilon_d L}{K_b}$$

where $T(0)$ and $T(L)$ are known temperatures at the seafloor and depth L beneath seafloor.

References:

Arriaga, M.A., Leap, D.I., 2006. Using solver to determine vertical groundwater velocities by temperature variations, Purdue University, Indiana, USA. Hydrogeol. J., 14, 253-263.

Ashi, J., Taira, A., 1993. Thermal structure of the Nankai accretionary prism as inferred from gas hydrate BSRs. In: Underwood, M.B. (Ed.), Thermal Evolution of the Tertiary Shimanto Belt, Southwest Japan: An Example of Ridge-Trench Interaction, vol. 273, pp. 137–149.

Baba, K., Yamada, Y., 2004. BSR's and associated reflections as an indicator of gas hydrate and free gas accumulation: an example of accretionary prism and forearc basin system along the Nankai Trough, off central Japan. Resource Geology 54, 11-24.

Bakulin, A., Grechka, V., Tsvankin, I. 2000. Estimation of fracture parameters from reflection seismic data--Part I: HTI model due to a single fracture set, Geophysics 65(6), 1788--1802.

Bastia, R., 2006. An overview of Indian sedimentary basins with special focus on emerging east coast deepwater frontiers. The Leading Edge 25, 818–829.

Bredehoeft, J.D., Papadopulos, I.S., 1965. Rates of vertical groundwater movement estimated from the earth's thermal profile. Water Resources Research 1, 325–328.

Bogdanov, Yu.A., Sagalevich, A.M., Vogt, P.R., Mienert, J., Sundvor, E., Crane, K., Lein, A. Yu., Egorov, A. V., Peresypkin, V. I., Cherkashev, G. A., Gebruk, A.V., Ginsburg, G. D., Voitov, D. V., 1999. The Haakon Mosby mud volcano in the Norwegian Sea: results of multidisciplinary studies with manned submersibles. Oceanology 39, 374-380.

Brooks, J.M., Cox, H.B., Bryant, W.R, Kennicutt II, M.C., Mann,R.G., Mc Donald, T.J., 1986. Association of gas hydrates and oil seepages in Gulf of Mexico. Organic Geochemistry 10, 221-234.

Caress, D.W., Chayes, D.N., 1996. Improved processing of hydrosweep DS multibeam data on the R/V Maurice Ewing. Marine Geophysical Researches 18, 631–650.

Collett, T. S., et al., 2008. Results of the Indian National Gas Hydrate Program Expedition 01 initial reports, report, Director General of Hydrocarbons, Ministry of Petroleum and Natural Gas, New Delhi.

Contreras, P., Grechka, V., Tsvankin, I., 1999. Moveout inversion of P-wave data for horizontal transverse isotropy, Geophysics 64(4), 1219-1229.

Cook, A., Goldberg, D., 2008. Extent of gas hydrate filled fracture planes: Implications for in situ methanogenesis and resource potential. Geophysical Research Letters 35(15), L15302.

Dallimore, S.R., Uchida T., Collett, T. S., 1999. Scientific Results from JAPEX/JNOC/GSC Mallik 2L-38 Gas Hydrate Research Well, Mackenzie Delta, Northwest Territories, Canada, Geological Survey of Canada Bulletin 544, 403 p.

Damuth, J.E., 1994. Neogene gravity tectonics and depositional processes on the deep Niger Delta continental margin. Marine and Petroleum Geology 11, 320–346.

Davie, M., Buffett, B., 2003. Sources of methane for marine gas hydrate: inferences from a comparison of observations and numerical models. Earth and Planetary Science Letters 206, 51--63.

Davis, E.E., Hyndman, R.D., Villinger, H., 1990. Rates of fluid expulsion across the northern Cascadian accretionary prism: constraints from new heat flow and multichannel seismic reflection data. Journal of Geophysical Research 95, 8869–8889.

Deyhle, A., Kopf, A., Frape, S., Hesse, R., 2004. Evidence for fluid flow in the Japan Trench forearc using isotope geochemistry (Cl, Sr, B): Results from ODP Site 1150. Island Arc **13**(1), 258--270.

Diaconescu, C.C., Knapp, J.H., 2000. Buried gas hydrates in the deepwater of the South Caspian Sea, Azerbijian: Implications for geohazards. Energy Exploration and Exploitation 18, 209-221.

Diaconescu, C. C., Kieckhefer, R. M., Knapp, J.H., 2001. Geophysical evidence for gas hydrates in the deeper water of the South Caspian Basin, Azerbijian. Marine and Petroleum Geology 18, 209-221.

Dickens, G. R., Paull, C. K., Wallace, P. The ODP Leg 164 Scientific Party., 1997. Direct measurements of in situ methane quantities in large gas-hydrate reservoir. Nature 385, 426-428.

Egeberg, P., Dickens, G., 1999. Thermodynamic and pore water halogen constraints on gas hydrate distribution at ODP Site 997 (Blake Ridge). Chemical Geology 153(1-4), 53--79.

Fisher, A.T., Hounslow, M.W., 1990. Transient fluid flow through the toe of the Barbados accretionary complex: constraints from ODP Leg 110 heat flow studies and simple models. Journal of Geophysical Research 95, 8845–8858.

Ganguly. N., Spence. G.D., Chapman. N.R., Hyndman. R.D., 2000. Heat flow variations from bottom simulating reflectors on the Cascadia margin. Marine Geology 164, 53–68.

Ginsburg, G.D., Mikov, A. V., Soloviev, V.A., Egorov, A. V., Cherkashev, G. A., Vogt, P.R., Crane, K., Lorenson, T. D., Khutorskoy, M.D., 1999. Gas hydrate accumulation at the Haakon Mosby mud volcano. Geo-Marine Letters 19, 57-67.

Grevemeyer, I., Villinger, H., 2001. Gas hydrate stability and the assessment of heat flow through continental margins. Geophysical Journal International 145(3), 647--660.

Grevemeyer, I., Diaz-Naveas, J.L., Ranero, C.R., Villinger, H.W., 2003. ODP Leg 202 Scientific Party, Heat flow over the descending Nazac plate in the central Chile, 32^{o}S to 41^{o}S: observations from ODP Leg 202 and the occurrence of natural gas hydrates. Earth and Planetary Science Letters 213, 193-211.

Gupta, S.K., 2006. Basin architecture and petroleum system of Krishna Godavari Basin, east coast of India. The Leading Edge 25, 830.

Haacke, R.R., Westbrook, G.K., Hyndman, R.D., 2007. Gas hydrate, fluid flow and free gas: Formation of the bottom-simulating reflector. Earth and Planetary Science Letters 261, 407-420.

Haacke, R., Westbrook, G., & Riley, M., 2008. Controls on the formation and stability of gas hydrate-related bottom-simulating reflectors (BSRs): A case study from the west Svalbard continental slope. Journal of Geophysical Research-Solid Earth 113(B5), B05104.

Helgerud, M. B., Dvorkin, J., Nur, A., Sakai, A., Collett, T., 1999. Effective wave velocity in marine sediments with gas hydrates: Effective medium modeling: Geophysical Research Letters 26, 2021-2024.

Hesse, R., Egeberg, P., Frape, S., 2006. Chlorine stable isotope ratios as tracer for pore-water advection rates in a submarine gas-hydrate field: implication for hydrate concentration. Geofluids 6(1), 1--7.

Hornbach, M., Ruppel, C., Saffer, D., Van Dover, C., Holbrook, W., 2005. Coupled geophysical constraints on heat flow and fluid flux at a salt diapir. Geophysical research letters 32(24), L24617.

Hovland, M., Lysne, D., Whiticar, M.J, 1995. Gas hydrate and sediment gas compostion , Hole 892A. In B. Carson, G.K. Westbrook, R.J. Musgrave, E.Suess (Eds), Proceddings of the Ocean drilling Program, Scientific Results, Vol. 146, pp.151-161.

Hovland, M., Gallagher, J., Clennell, M., Lekvam, K., 1997. Gas hydrate and free gas volumes in marine sediments: Example from the Niger Delta front. Marine and Petroleum Geology 14(3), 245--255.

Hutchison, I., 1985. The effect of sedimentation and compaction on ocean heat flow. Geophysical Journal of.Royal Astronomical Society 82, 439-459.

Hyndman, R., Davis, E., 1992. A mechanism for the formation of methane hydrate and seafloor bottom-simulating reflectors by vertical fluid expulsion. Journal of Geophysical Research 97 (5)., 7025–7041.

Hyndman, R.D., Spence, G.D., 1992. A Seismic Study of Methane Hydrate Marine Bottom Simulating Reflectors. Journal of Geophysical Research 97:6683—6698.

Hyndman, R.D., Spence, G.D., Chapman, R., Riedel, M., Edwards, R.N., 2001. Geophysical studies of marine gas hydrate in the northern Cascadia. In: Paull , C.K., Dillon, W.P.(Eds), Natural gas hydrates : Occurrence, Distribution and Detection. American Geophysical Union 124, PP273-296.

Judd, A., Hovland, M., 2007. Seabed Fluid Flow: The Impact of Geology, Biology and the Marine Environment. Cambrige University Press.

Kaul, N., Rosenberger, A., Villinger, H., 2000. Comparison of measured and BSR-derived heat flow values, Makran accretionary prism, Pakistan. Marine Geology 164, 37–51.

Lachenbruch, A.H., 1968. Rapid estimation of the topographic disturbance to superficial thermal gradients. Reviews of Geophysics 6, 365–400.

Land, L.A., Paull, C.K., 2001. Thermal gradients as a tool for estimating groundwater advective rates in a coastal estuary: White Oak River, North Carolina. J. Hydrol., 248, 198-225.

Lee, M., Collett, T., 2009. Gas hydrate saturations estimated from fractured reservoir at Site NGHP-01-10, Krishna-Godavari Basin, India. Journal of Geophysical Research 114(B7), B07102.

Lee, M.W., Dillon, W.P., 2001. Amplitude blanking related to pore-filling of gas hydrate in sediments. Marine Geophysical Researches 22, 101-109.

Lee, M.W., 2009. Anisotropic velocities of gas hydrate-bearing sediments in fractured reservoirs. US Geological Survey Scientific Investigations Report 2009–5141, 13 p.

Lu, Z., Tomaru, H., Fehn, U., 2008. Iodine ages of pore waters at Hydrate Ridge (ODP Leg 204), Cascadia Margin: Implications for sources of methane in gas hydrates. Earth and Planetary Science Letters 267(3-4), 654--665.

MacDonald, I.R., Guinasso, N.L., Sassen, R., Brooks, J.M., Lee,L., Scott, K.T., 1994. Gas hydrates that breaches the sea-floor on the continental slope of Gulf of Mexico. Geology 22, 699-702.

Mann, D., Kukowski, N., 1999. Numerical modelling of focused fluid flow in the Cascadia accretionary wedge. Journal of Geodynamics 27, 359-372.

Matsumoto, R., Takedomi Y. and Wassada H., 2001. Exploration of marine gas hydrates in Nankai Trough, offshore Central Japan. AAPG Annual Convention, Official Program 10, A128.

Mazumdar, A., Dewangan, P., Joao, H.M., Peketi, A., Khosla, V.R., Kocherla, M., Badesab, F.K., Joshi, R.K., Roxanne, P., Ramamurty, P.B., Karisiddaiah, S.M., Patil, D.J., Dayal, A.M., Ramprasad, T., Hawkesworth, C.J., Avanzinelli, R., 2009. Evidence of paleo–cold seep activity from the Bay of Bengal, offshore India. Geochemistry Geophysics Geosystems 10(6), 15 pp, doi:10.1029/2008GC002337.

Miles, P., 1995. Potential distribution of methane hydrate beneath the European continental margins. Geophysical Research Letters 22(23), 3179--3182.

Milkov, A.V., Sassen, R., 2000. Thickness of gas hydrate stability zone, Gulf of Mexico continental slope. Marine and Petroleum Geology 17, 981-991.

Milkov, A.V., Sassen, R., 2001. Estimate of gas hydrate resource, northwestern Gulf of Mexico continental slope. Marine Geology 179, 71-83.

Milkov, A., Sassen, R., 2002. Economic geology of offshore gas hydrate accumulations and provinces. Marine and Petroleum Geology 19(1), 1--11.

Minshull, T.A., White, R., 1989. Sediment composition and fluid migration in the Makran accretionary prism. Journal of Geophysical Research 94, 7387-7402.

Pecher, I., Ranerco, C.R., VonHuence, R., Minshull, T.A., Singh,S.C., 1998. The nature and distribution of bottom simulating reflector at the Costa Rica convergent margin. Geophysical Journal International 133, 219.

Pecher, I., Henrys, S., Wood, W., Kukowski, N., Crutchley, G., Fohrmann, M., Kilner, J., Senger, K., Gorman, A., Coffin, R., Richard B., Greinert, J., Faure, K., 2009. Focused fluid flow on the Hikurangi Margin, New Zealand—Evidence from possible local upwarping of the base of gas hydrate stability. Marine Geology. doi:10.1016/j.margeo.2009.10.006.

Pflaum, R. C., Brooks, J.M., Cox, H. B., Kennicutt, M.C. II., Sheu, D.D., 1986. Molecular and isotopic analysis of core gases and gas hydrates, DSDP Leg 96. In A.H.Bouma, J. M, Coleman, A.W. Meyer (Eds.), Initial Report of the Deep Sea Drilling Prjoect, 96. Washington, Dc: US Government Printing Office. PP 781-784.

Powell, C.M., Roots, S.R., Veevers, J.J., 1988. Pre-breakup continental extension in east Gondwanaland and the early opening of the eastern Indian Ocean. Tectonophysics 155, 261–283.

Prabhakar, K.N., Zutshi, P.L., 1993. Evolution of southern part of Indian east coast basins. Journal of Geological Society of India 41, 215–230.

Ramana, M.V., Nair, R.R., Sarma, K.V.L.N.S., Ramprasad, T., Krishna, K.S., Subrahmanyam, V., D'Cruz, M., Subrahmanyam, C., Paul, J., Subrahmanyam, A.S., Sekhar, D.V.C., 1994. Mesozoic anomalies in the Bay of Bengal. Earth and Planetary Science Letters 121, 469–475.

Ramana, M.V., Ramprasad, T., Desa, M., Sathe, A.V., Sethi, A.K., 2006. Gas hydrate-related proxies inferred from multidisciplinary investigations in the Indian offshore areas. Current Science 91(2), 183-189.

Ramana, M.V., Ramprasad, T., Paropkari, A.L., Borole, D.V., Ramalingeswara Rao, B., Karisiddaiah, S.M., Desa, M., Kocherla, M., Joao, H.M., Lokabharati, P., Gonsalves, Maria-Judith, Pattan, J.N., Khadge, N.H.,

Prakash Babu, C., Sathe, A.V., Kumar, P., Sethi, A. K., 2009. Multidisciplinary investigations exploring indicators of gas hydrate occurrence in the Krishna–Godavari Basin offshore, east coast of India. Geo-Marine Letters 29(1), 25-38.

Ramprasad, T., Dewangan, P., Ramana, M.V., Mazumdar, A., Karisiddaiah, S.M., Ramya, E.R., Sriram, G., 2011. Evidence of Slumping/Sliding in Krishna-Godavari Offshore Basin due to gas/fluid movements. Marine and Petroleum Geology. doi:10.1016/j.marpetgeo.2011.02.007

Rao, G.N., 1993. Geology and hydrocarbon prospects of East Coast sedimentary basin of India with special reference to Krishna-Godavari Basin. Journal of Geological Society of India 41, 444–454.

Rao, G.N., 2001. Sedimentation, stratigraphy, and petroleum potential of Krishna-Godavari Basin, East Coast of India. AAPG Bulletin 85, 1623–1643.

Rao, G.N., Mani, K.S., 1993. A study on generation of abnormal pressures in Krishna-Godavari basin. Indian Journal of Petroleum Geology 2, 20–30.

Riedel, M., Collett, T.S., Kumar, P., Sathe, A.V., Cook, A., 2010. Seismic imaging of a fractured gas hydrate system in the KrishnaeGodavari Basin offshore India. Marine and Petroleum Geology 27, 1476–1493.

Ruppel, C., 1997. Anomalously cold temperatures observed at the base of the gas hydrate stability zone, U.S. Atlantic passive margin. Geology 25, 699-704.

Ruppel, C., Kinoshita, M., 2000. Heat, methane, and energy flux in an active margin gas hydrate province, offshore Costa Rica. Earth and Planetary Science Letters 179, 153- 165.

Sassen , R., Sweet, S.T., Mikov, A.V., Defretias, D.A., Salata, G.G., McDade, E.C., 1999. Geology and geochemistry of gas hydrates, central Gulf of Mexico continental slope. Transactions Gulf Coast Association of Geological Societies 49,462-468.

Sassen , R., Losh, S., Cathles, L., Roberts, H., Whelan, J.K.., Mikov, A.V., Sweet,S.T., Defretias, D.A., 2001. Massive Vein-filling gas hydrate: Relation to ongoing gas migration from the deep subsurface Gulf of Mexico. Marine and Petroleum Geology 18, 551-560.

Scotese, C.R., Gahagan, L.M., Larson, R.L., 1988. Plate tectonic reconstructions of the Cretaceous and Cenozoic ocean basins. Tectonophysics 155, 27–48.

Shankar, U., Riedel, M., 2010. Seismic and heat flow constraints from the gas hydrate system in the Krishna-Godavari Basin, India', Marine Geology, doi:10.1016/j.margeo.2010.06.006.

Singh, S.C., Minshull, T.A., Spence, G.D., 1993. Velocity structure of a gas hydrate reflector. Science 260, 204–207.

Sloan, E.D., 1990. Clathrate Hydrates of Natural Gases: New York, Marcel Dekker, Inc., 641 p.

Stallman, R.W., 1963. Computation of ground-water velocity from temperature data. USGS Water supply Paper 1544-H, 36-47.

Stein, C., Stein, S., 1994. Constraints on hydrothermal heat flux through the oceanic lithosphere from global heat flow. Journal of Geophysical Research 99, 3081–3095.

Subrahmanyam, C., Chand, S., 2006. Evolution of the passive continental margins of India a geophysical appraisal. Gondwana Research 10(1-2), 167--178

Suess,E., Torres,M.E., Bohrmann,G., Collier, R.W., Grienert, J., Linke, P., Rehder, G., Trehu, A.M., Wallmann, K., Winckler, G., Zuleger, E., 1999. Gas hydrate destabilization: enhanced dewatering, benthic material turnover and large methane plumes at the Cascadia convergent margin. Earth and Planetary Science Letters 170, 1-15.

Suess, E., Torres, M.E., Bohrmann, G., Collier, R.W., Rickert, D., Godlfinger, C., Linke, P., Heuser, A., Sahling, H., Heeschen, K., Jung, C., Nakamura, K., Greinert, J., Pfannkuche, O., Trehu, A., Klinkhammer, G., Whiticar, M.J., Eisenhauer, A., Treichert, B., Elvert, M., 2001. Sea floor methane hydrates at Hydrate Ridge, Cascadia Margin. In C.K. Paull, W.P.Dillon, Natural gas hydrates: Occurrence , distribution, and dynamics, AGU Monograph Series24, 87-98.

Taylor, M., Dillon, W., Pecher, I., 2000. Trapping and migration of methane associated with the gas hydrate stability zone at the Blake Ridge Diapir: new insights from seismic data, Marine Geology 164 (1-2), 79--89.

Townend, J., 1997. Estimates of conductive heat flow through bottom-simulating-reflectors on the Hikurangi and southwest Fiordland continental margins, NewZealand. Marine Geology 141, 209–220.

Tsvankin, I., 1997. Reflection moveout and parameter estimation for horizontal transverse isotropy. Geophysics 62(2), 614--629.

Trehu, A.M., Toress, M.E., Moore, G.F., Suess, E., Bohrmann, G., 1999. Temporal and spatial evolution of a gas hydrate-bearing accretionary ridge on the Oregon continental margin. Geology 27, 939-942.

Vijayalakshmi, K.G., 1988. Miocene depositional systems in thrust areas in Krishna-Godavari basin. Bulletin of Oil and Natural Gas Corporation 25(2), 1-10.

Wu, S., Bally, A.W., 2000. Slope tectonics-comparisons and contrasts of structural styles of salt and shale tectonics of the northern Gulf of Mexico with shale tectonics of Offshore Nigeria in Gulf of Guinea. Geophysical Monograph 115, 151–172.

Xu, W., Ruppel, C., 1999. Predicting the occurrence, distribution, and evolution of methane gas hydrate in porous marine sediments. Journal of Geophysical Research 104, 5081-5096.

Zwart, G., Moore, J., Cochrane, G.,1996. Variations in temperature gradients identify active faults in the Oregon accretionary prism. Earth and Planetary Science Letters 139(3-4), 485--495.

Figures Caption

Fig. 1. Location map of the study area in KG offshore basin along with the regional tectonics setting showing the horst and graben structures (Rao, 2001; Bastia, 2006) onshore KG basin, Bay of Bengal. The zoom out of the study area with multibeam bathymetry is shown in Fig. 1b. The illustrated seismic lines, sub-bottom profiler, and high resolution sparker data are illustrated in the bathymetry map. The illustrated seismic lines are annotated with CDP numbers and the NGHP sites drilled onboard JOIDES Resolution (NGHP-01-10/21/12/13/03) are highlighted on the map. The location of NGHP-01-03 site where no significant presence of gas hydrate is observed is also shown in the map.

Fig. 2. Analysis of an inline seismic profile. A) time migrated multi-channel seismic data; B) Black line shows the BSR derived geothermal gradient (GTG) and red line shows the normalized amplitude of the BSR; C) The interpreted seismic section with difference horizons marked with different color, light blue color represents the interpreted BSR; D) The velocity model obtained after conventional semblance analysis of multi-channel seismic data, the water bottom and BSR horizons are highlighted on the velocity model. A drop in interval velocity is observed below the BSR whereas several high velocity patches are observed in the GHSZ.

Fig. 3. Analysis of a crossline seismic profile similar to Fig. 2. The NGHP-01-10 site is highlighted on the interpreted section. A small piercement like feature is observed between CDPs 250-350 at around 1.7 s. The same feature is observed in the velocity model by anomalous increase in velocity.

Fig. 4. A) Seismic derived seafloor map along with the traces of major fault system as well as the locations of drilling/coring sites. NGHP-01-10 site passes through fault F_4 while the NGHP-01-12 and 13 sites are close to fault F_5; B) Contour plot of orange horizon along with the traces of major faults. Fault F_1 and F_3 can be clearly observed on this map.

Fig. 5. The SBP data close to the observed topographic mound. A) Central portion of the mound located close to site 10. The surface imprints of fault F3 and F4 are clearly visible; B) Northern part of the mound; C) southern part of the mound. The high amplitude and lack of any internal reflection possible suggest gas masking. The location of the SBP profiles is shown in Fig. 1b.

Fig. 6. High resolution seismic profile acquired onboard Sagar Nidhi. A) The HRS data close to the inline seismic profile shown in Fig. 2. The major faults are transferred from the interpreted MCS profile and it agrees with the HRS data. The prominent zone of seismic blanking is observed in the data. B) The HRS data close to the crossline seismic profile shown in Fig. 3. The HRS data also confirms major fault system. A less prominent seismic blanking is observed for this profile. A faint BSR reflector is observed in HRS data at certain location close to the fault system. The CDP number on HRS data represents the closest CDP number of MCS data

Fig. 7. Temperature profile obtained from CTD data in KG offshore basin. The solid, dashed and dashed-dot lines show the temperature profile for difference CTD locations. In the zone of interest (1000-1200 mbsf), the temperature profiles are almost same for all three stations.

Fig. 8. BSR derived geothermal gradient and the interpreted gas horizon in the study area. A) BSR derived GTG is superimposed by the traces of fault system. An abnormal increase in GTG is observed close to the fault system at the center of the mound close to the fault system. B) The interpreted gas horizon from the available seismic lines with traces of the fault system. The GTG distribution appears to be symmetric with respect to the interpreted gas bearing horizon with the maximum GTG anomaly occurring atop the gas horizon.

Fig. 9. Moveout corrected CDP gather from the seismic profile shown in Fig. 2 close to CDP 710. A) Moveout correct CDP gather with the velocity required to explain the observed GTG (45 ^{o}C/km) . The moveout is flat for BSR; B) Moveout corrected CDP gather for the velocity that is required for the background GTG (40 ^{o}C/km). A significant moveout is observed at the BSR depth suggesting that the velocity is incorrect.

Fig. 10. Regional geothermal gradient and topographic correction along the inline seismic line. a) seafloor topography and its 2D plane approximation, b) regional geothermal gradient and the estimated topographic correction. The correction suggests decrease in GTG at the top of the mound and increase in GTG at the valley.

Fig. 11. GTG variation along the inline seismic line for different salinities assuming a constant BSR depth. The salinity value in g/l is indicated by number for different curves. An increase in salinity from 35 g/l to 50 g/l is required to explain the observed variation in GTG due to salinity effect.

Fig. 12. Depth dependent temperature profiles for various stratigraphic sequences and Darcy velocities. The dot represents the depth and temperature at NGHP-01-10 site. We estimated the fluid advection rates for Upper Cretaceous sequence to be ~0.37 mm/yr, Paleocene sequence to be ~0.4 mm/yr, Eocene sequence to be ~0.5 mm/yr and Miocene sequence to be ~0.6 mm/yr.

Table Caption

Table 1. Parameters used for calculating fluid advection rates assuming 1-D analytical solution of the differential equation for simultaneous conductive and advective heat transport in a homogenous, isotropic, and fully saturated medium (Bredehoeft and Papadopulos, 1965).

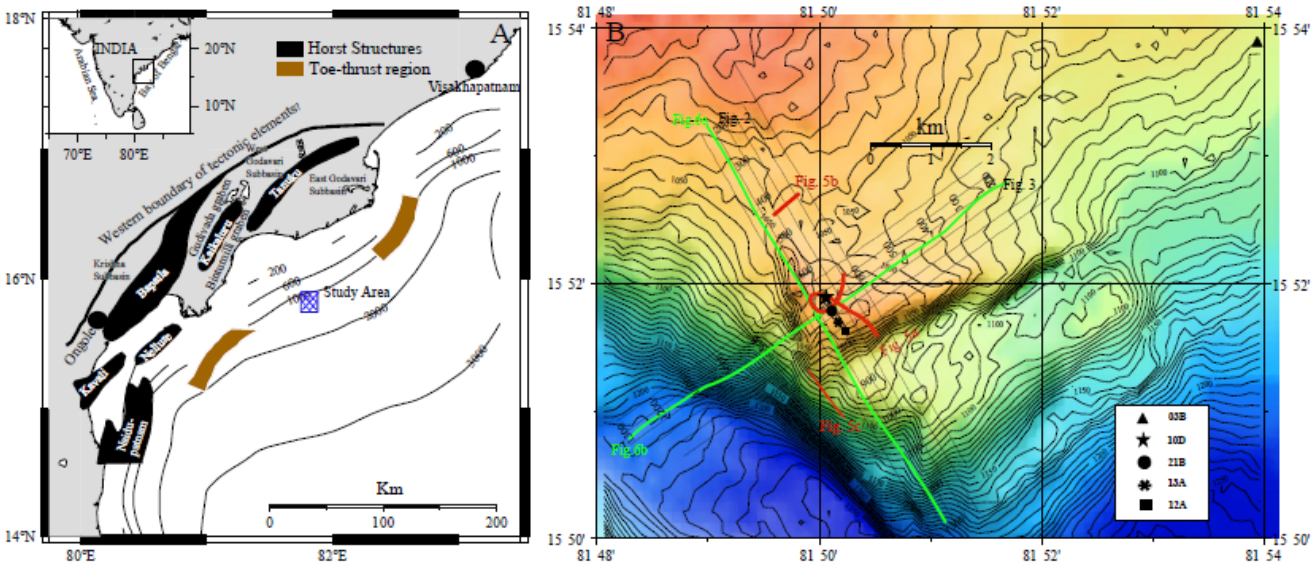
A
B
INDIA
Arabian Sea
Bay of Bengal
20°N
10°N
70°E
80°E
Horst Structures
Toe-thrust region
Visakhapatnam
Western boundary of tectonic elements
Krishna Subbasin
Godavari Subbasin
East Godavari Subbasin
Tanuku
Bapatla
Challapalli
Pasarlapudi
Kakinada
Ongole
Kavali
Nellore
Nidadavolu
Study Area
Km
0
100
200
18°N
16°N
14°N
80°E
82°E
81 48'
81 50'
81 52'
81 54
15 54'
15 52'
15 50'
Fig.2
Fig.3
Fig.4a
Fig.4b
Fig.5a
Fig.5b
km
1
2
03B
10D
21B
13A
12A

Fig.1.

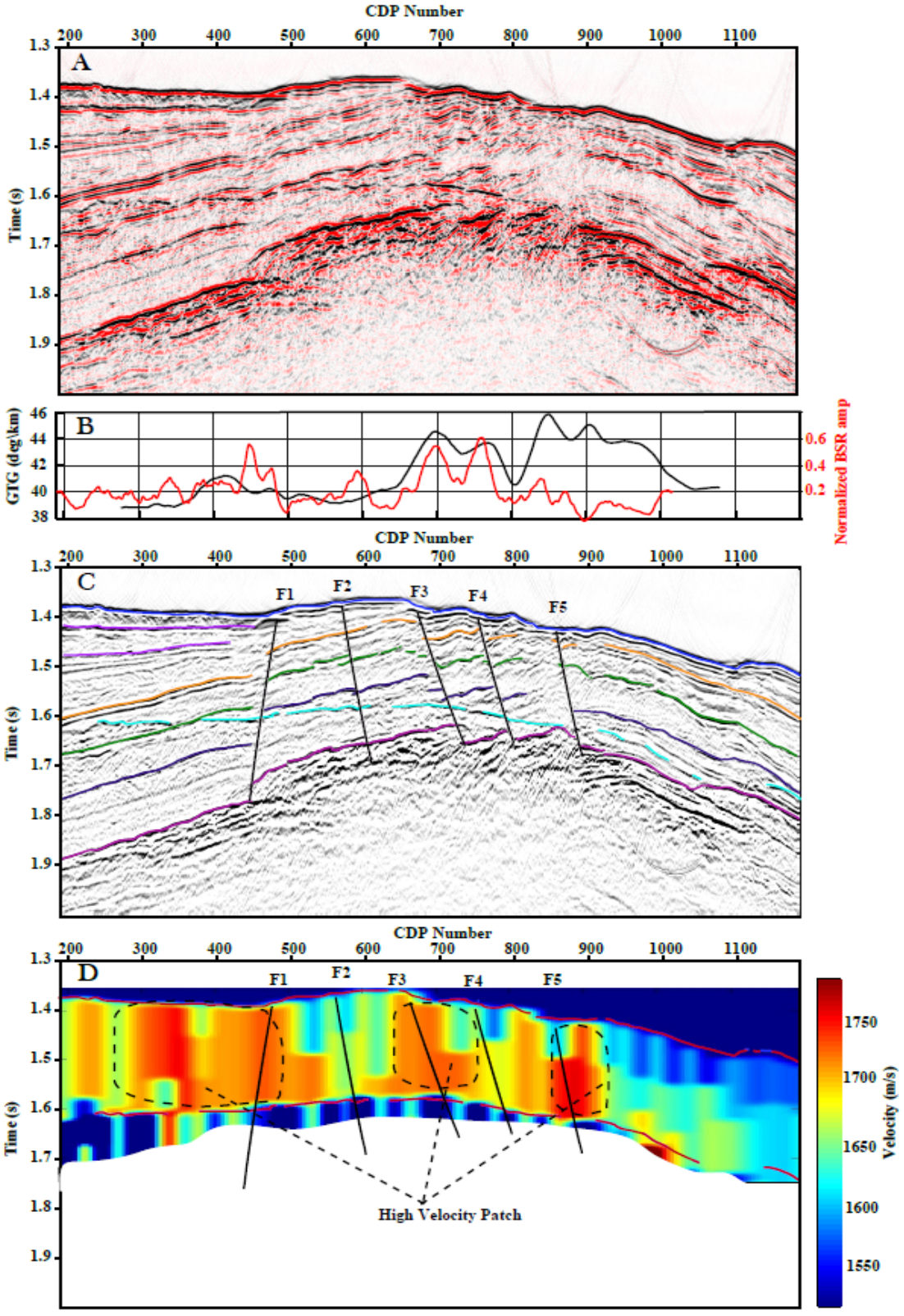
CDP Number
200
300
400
500
600
700
800
900
1000
1100
A
Time (s)
1.3
1.4
1.5
1.6
1.7
1.8
1.9
B
GTG (deg\km)
46
44
42
40
38
0.6
0.4
0.2
Normalized BSR amp
C
F1
F2
F3
F4
F5
D
High Velocity Patch
1750
1700
1650
1600
1550
Velocity (m/s)

Fig.2.

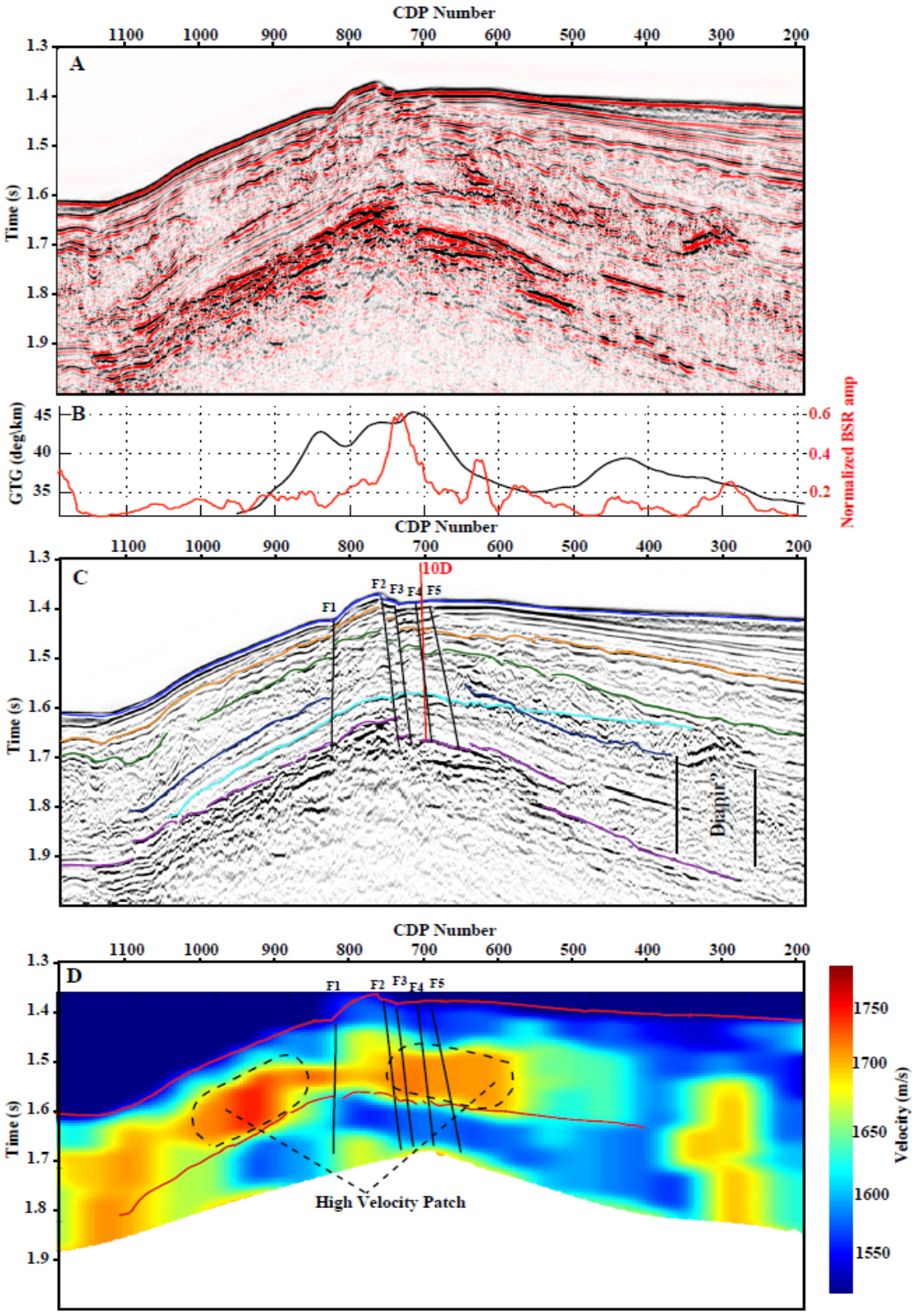
CDP Number
1100 1000 900 800 700 600 500 400 300 200
A
Time (s)
1.3 1.4 1.5 1.6 1.7 1.8 1.9
B
GTG (deg\km)
45 40 35
0.6 0.4 0.2
Normalized BSR amp
CDP Number
C
10D
F1 F2 F3 F4 F5
Diapir?
Time (s)
CDP Number
D
F1 F2 F3 F4 F5
High Velocity Patch
Time (s)
1750 1700 1650 1600 1550
Velocity (m/s)

Fig.3.

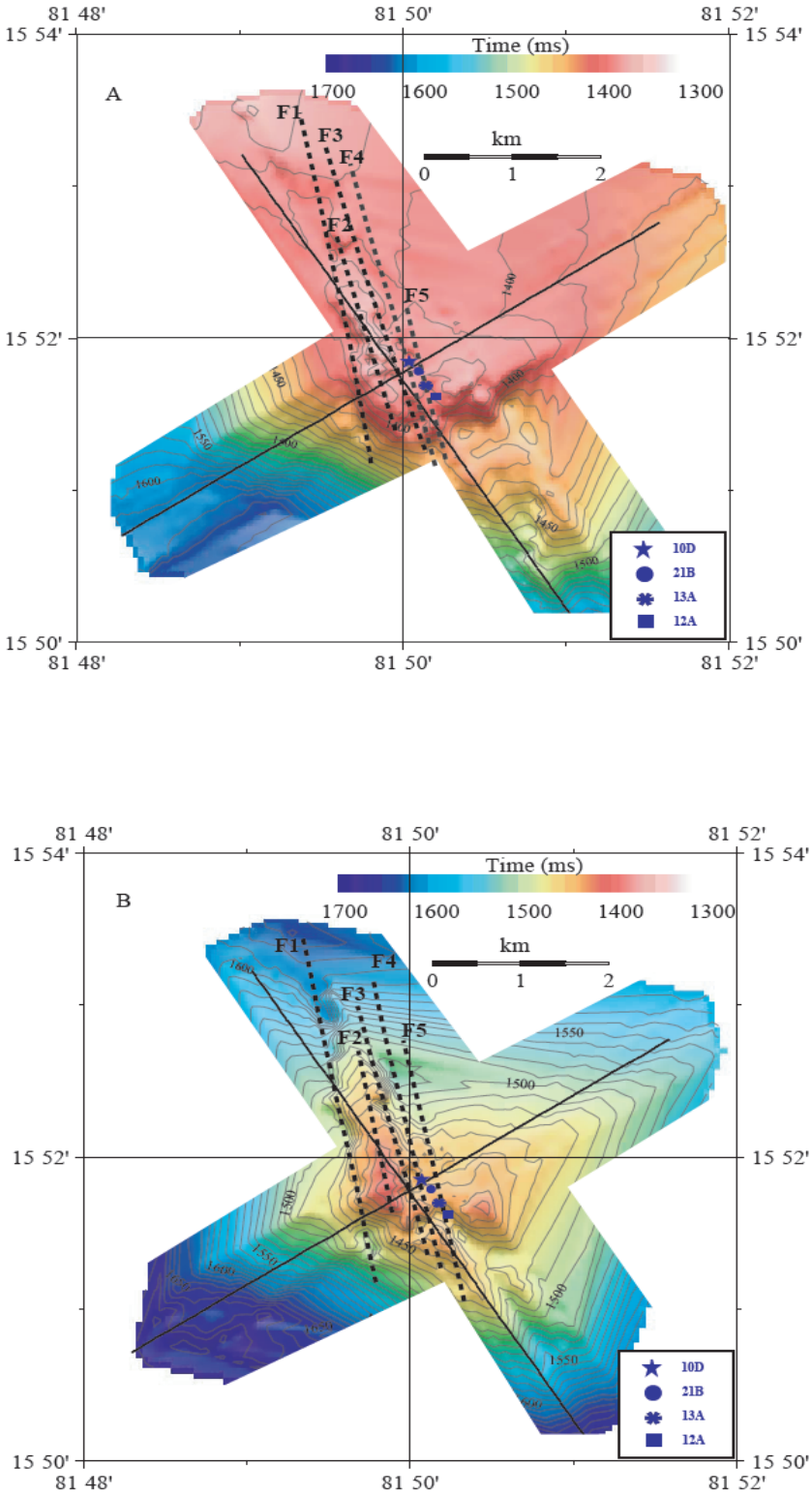
A
Time (ms)
1700
1600
1500
1400
1300
km
0
1
2
F1
F3
F4
F2
F5
10D
21B
13A
12A
81 48'
81 50'
81 52'
15 54'
15 52'
15 50'
B
Time (ms)
1700
1600
1500
1400
1300
km
0
1
2
F1
F4
F3
F2
F5
10D
21B
13A
12A
81 48'
81 50'
81 52'
15 54'
15 52'
15 50'

Fig.4.

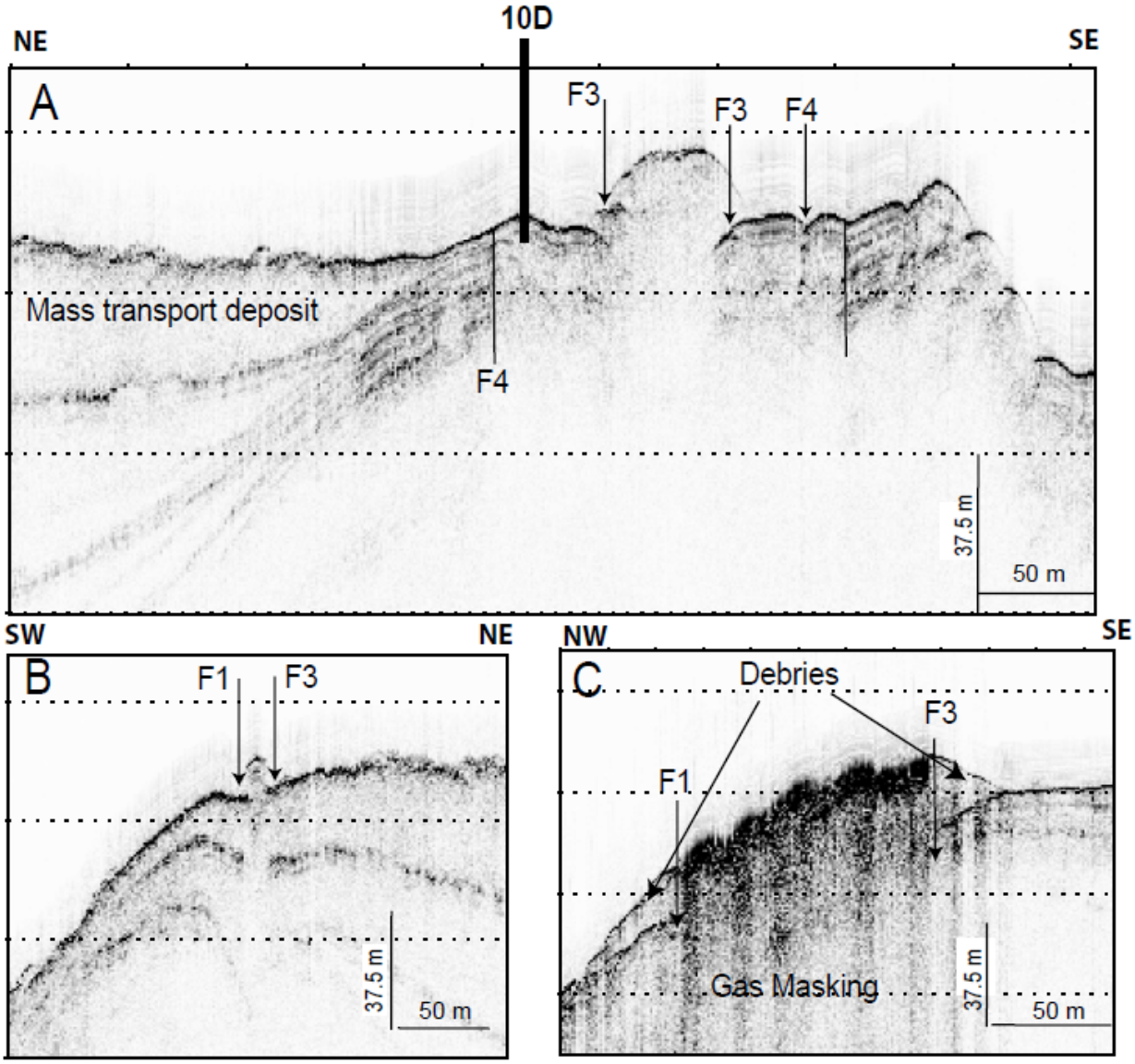
10D
NE
SE
A
F3
F3
F4
Mass transport deposit
F4
37.5 m
50 m
SW
NE
B
F1
F3
37.5 m
50 m
NW
SE
C
Debries
F3
F1
Gas Masking
37.5 m
50 m

Fig.5.

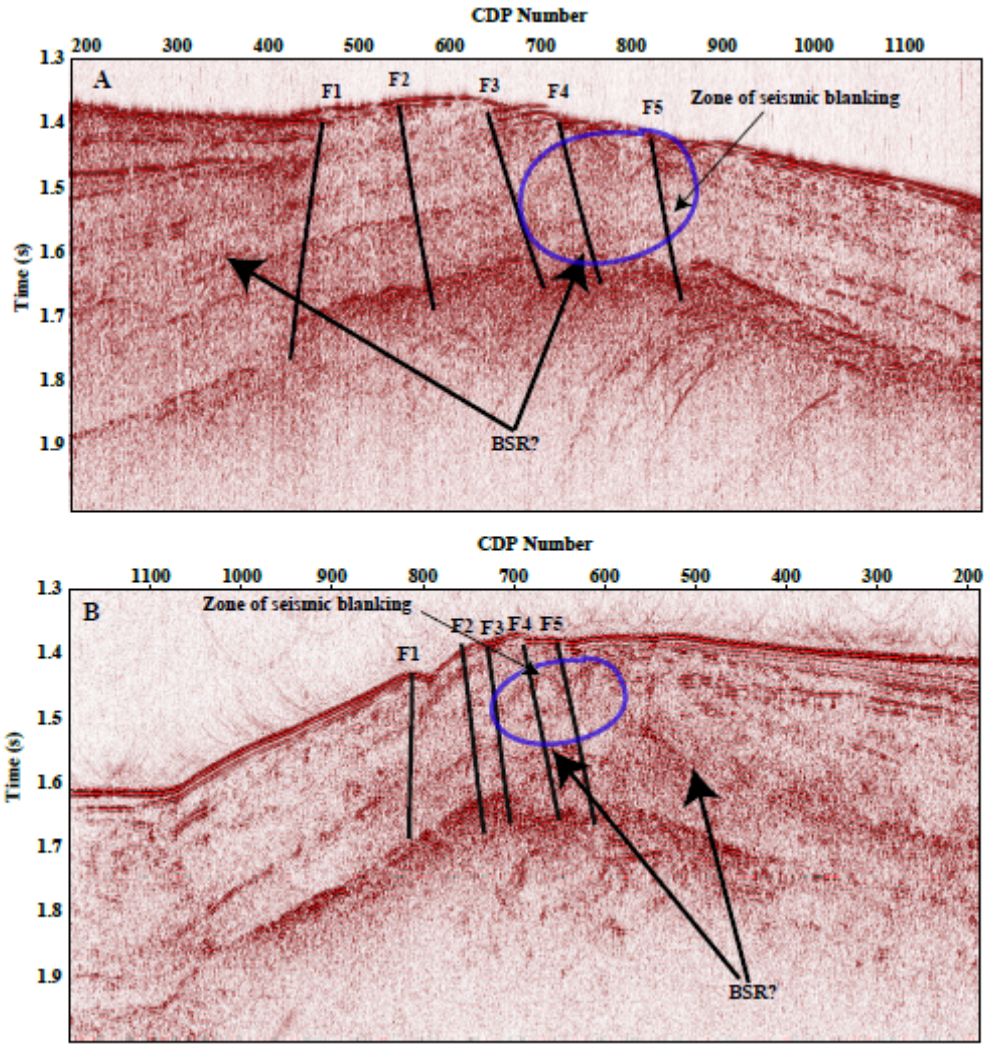
CDP Number
200
300
400
500
600
700
800
900
1000
1100
A
F1
F2
F3
F4
F5
Zone of seismic blanking
Time (s)
1.3
1.4
1.5
1.6
1.7
1.8
1.9
BSR?
CDP Number
1100
1000
900
800
700
600
500
400
300
200
B
Zone of seismic blanking
F1
F2
F3
F4
F5
Time (s)
1.3
1.4
1.5
1.6
1.7
1.8
1.9
BSR?

Fig.6.

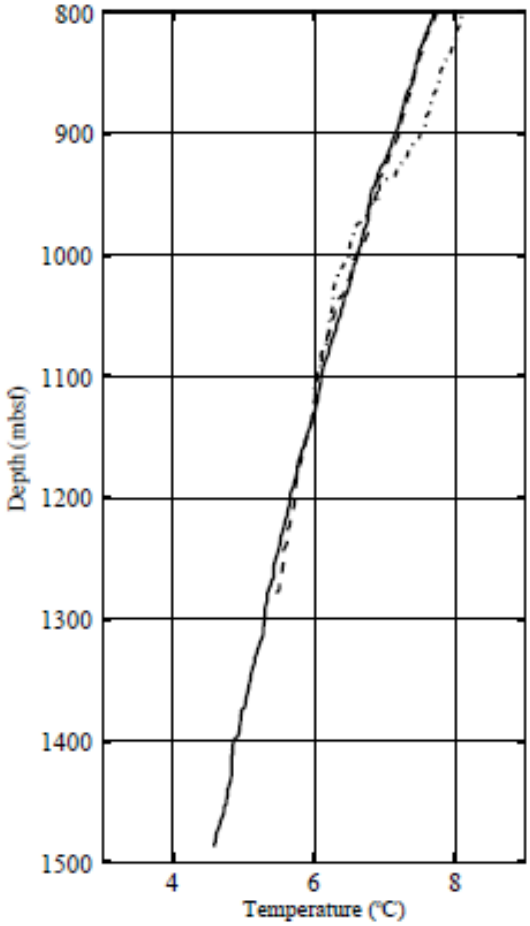
800
900
1000
1100
1200
1300
1400
1500
Depth (mbsf)
4
6
8
Temperature (°C)

Fig.7.

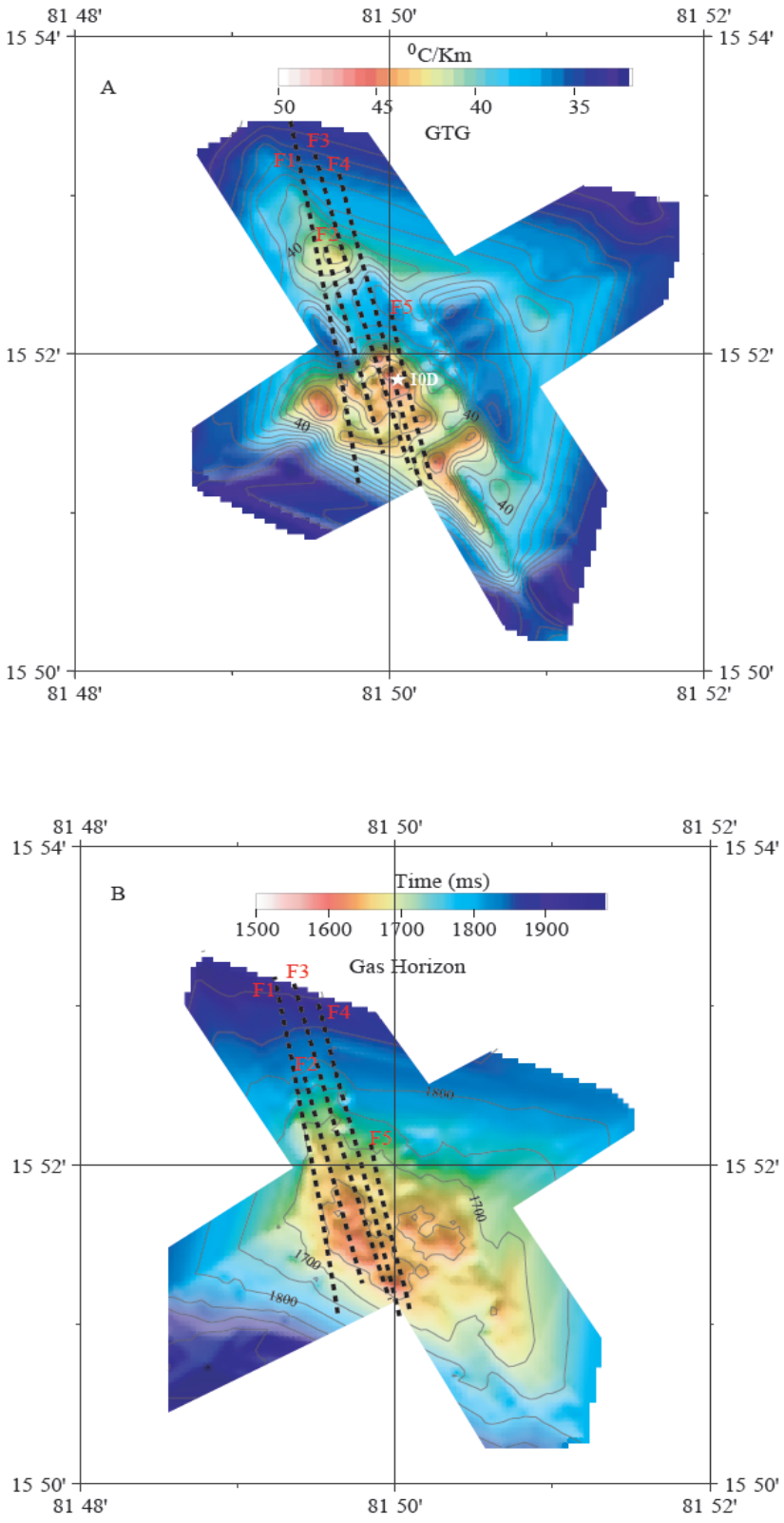
A
^{0}C/Km
50
45
40
35
GTG
F1
F2
F3
F4
F5
10D
40
B
Time (ms)
1500
1600
1700
1800
1900
Gas Horizon
81 48'
81 50'
81 52'
15 54'
15 52'
15 50'

Fig.8.

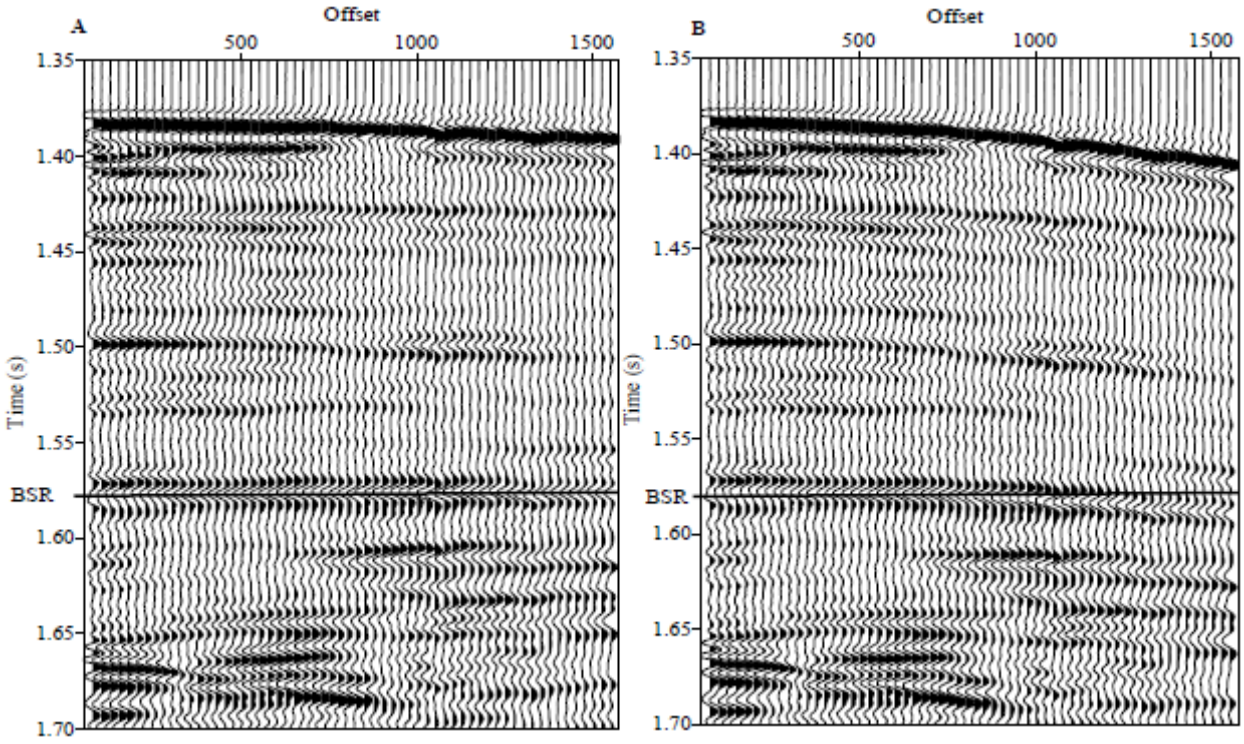
A
Offset
500
1000
1500
1.35
1.40
1.45
1.50
1.55
BSR
1.60
1.65
1.70
Time (s)
B
Offset
500
1000
1500
1.35
1.40
1.45
1.50
1.55
BSR
1.60
1.65
1.70
Time (s)

Fig.9.

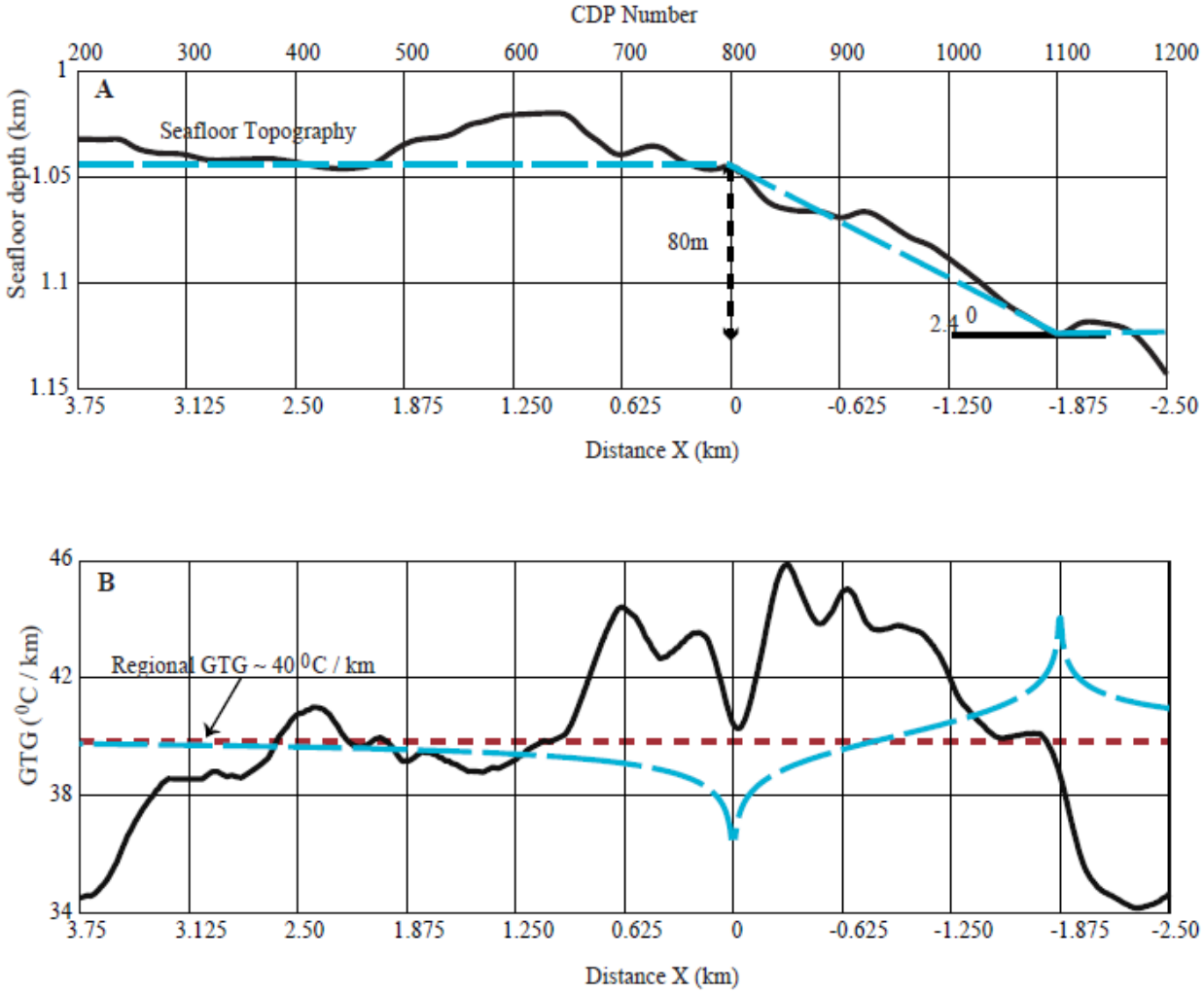
CDP Number
200
300
400
500
600
700
800
900
1000
1100
1200
A
Seafloor Topography
Seafloor depth (km)
1
1.05
1.1
1.15
80m
2.4 0
3.75
3.125
2.50
1.875
1.250
0.625
0
-0.625
-1.250
-1.875
-2.50
Distance X (km)
B
Regional GTG ~ 40 0C / km
GTG (0C / km)
46
42
38
34
Distance X (km)

Fig.10.

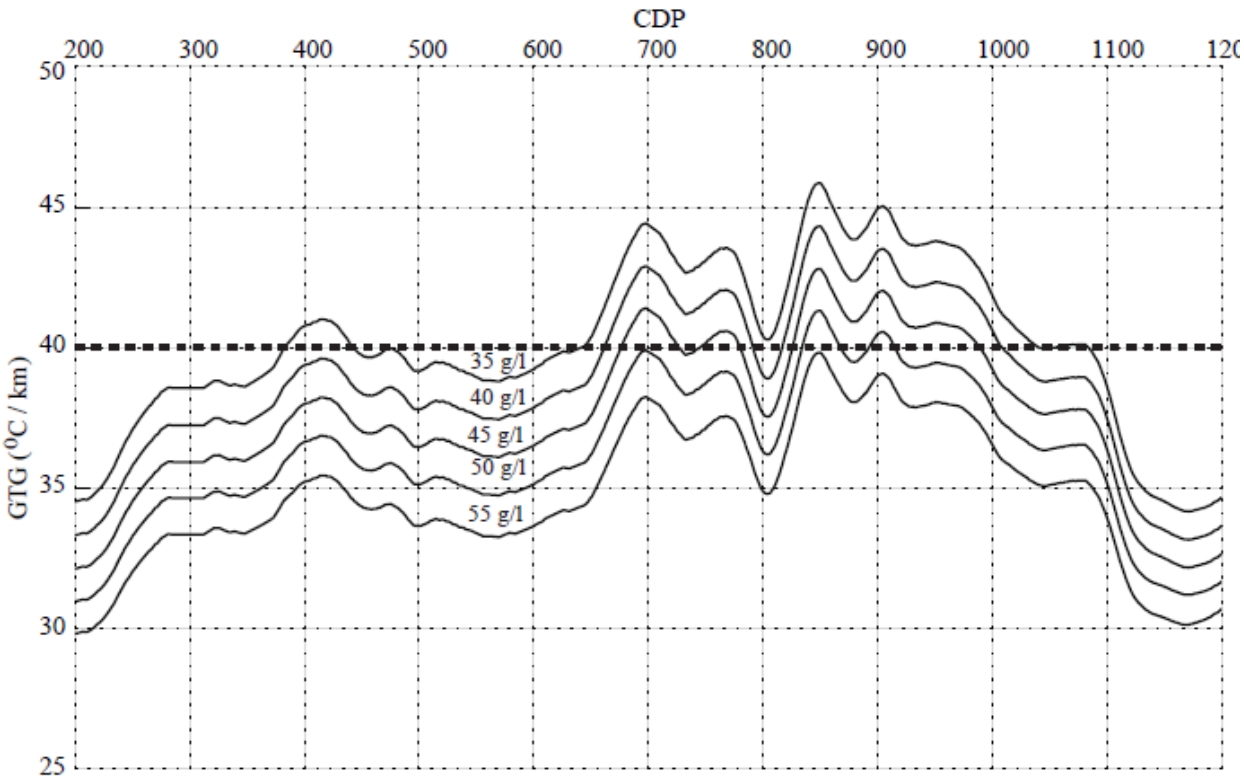
CDP
200
300
400
500
600
700
800
900
1000
1100
50
45
40
35
30
25
GTG (°C / km)
35 g/l
40 g/l
45 g/l
50 g/l
55 g/l

Fig.11.

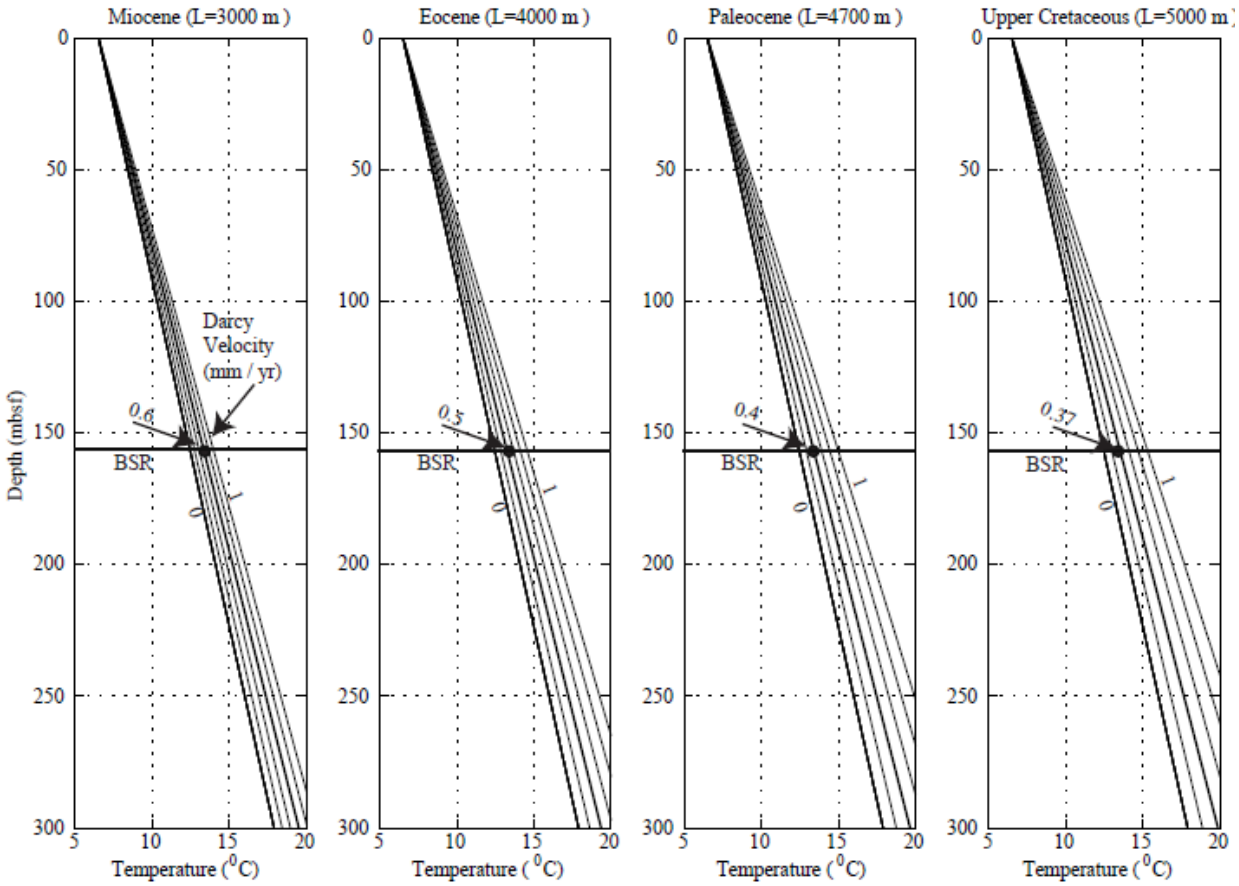

Fig.12.

T (0) (temperature at seafloor in °C)	6.4
dT/dz (Background geo-thermal gradient in ^{o}C/km)	38
K_b(Bulk thermal conductivity of sediment in W m^{-1} K^{-1})	0.82
C_f (specific heat capacity of pore fluid in J kg^{-1} K^{-1})	4180
ρ_f (density of pore fluid in kg/m^3)	1038
T (L) (temperature at depth L)	

Table 1